

ALPINE: a climbing robot for operations in mountain environments

Michele Focchi^{a,g,*}, Andrea Del Prete^b, Daniele Fontanelli^c, Marco Frego^d, Angelika Peer^e, Luigi Palopoli^f

^a*Dipartimento di Ingegneria e Scienza dell'Informazione (DISI), University of Trento, via Sommarive 9, 38123, Trento, Italy*

^b*Dipartimento di Ingegneria Industriale (DII), University of Trento, via Sommarive 9, 38123, Trento, Italy*

^c*Dipartimento di Ingegneria Industriale (DII), University of Trento, via Sommarive 9, 38123, Trento, Italy*

^d*Faculty of Engineering, Free University of Bozen-Bolzano, via Volta 13/A, 39100, Bolzano-Bozen, Italy*

^e*Faculty of Engineering, Free University of Bozen-Bolzano, via Volta 13/A, 39100, Bolzano-Bozen, Italy*

^f*Dipartimento di Ingegneria e Scienza dell'Informazione (DISI), University of Trento, via Sommarive 9, 38123, Trento, Italy*

^g*Dynamic Legged Systems, Istituto Italiano di Tecnologia (IIT), Genova, via San Quirico 19d, 16163, Genova, Italy*

Abstract

Mountain slopes are perfect examples of harsh environments in which humans are required to perform difficult and dangerous operations such as removing unstable boulders, dangerous vegetation or deploying safety nets. A good replacement for human intervention can be offered by climbing robots. The different solutions existing in the literature are not up to the task for the difficulty of the requirements (navigation, heavy payloads, flexibility in the execution of the tasks). In this paper, we propose a robotic platform that can fill this gap. Our solution is based on a robot that hangs on ropes, and uses a retractable leg to jump away from the mountain walls. Our package of mechanical solutions, along with the algorithms developed for motion planning and control, delivers swift navigation on irregular and steep slopes, the possibility to overcome or travel around significant natural barriers, and the ability to carry heavy payloads and execute complex tasks. In the paper, we give a full account of our main design and algorithmic choices and show the feasibility of the solution through a large number of physically simulated scenarios.

Keywords: Planning, Control, Climbing Robot, Trajectory optimization

Supplementary Material

- Video of experimental results is available at: <https://youtu.be/FqsREaoe-28>
- Code available at: https://github.com/mfocchi/climbing_robots2 (with source code used to generate all the figures in Section 6).

1. Introduction

Mountain environments are extremely vulnerable to climate change and often subject to landslides, floods and avalanches. Such ruinous events endanger a large number of economic activities (first and foremost tourism and agriculture) and put at risk the very survival of small towns and villages. Any realistic strategy to counter these risks is necessarily based on constant monitoring and on regular maintenance operations on the mountains slopes. Such

activities include detaching from the mountain walls dangerous boulders (a.k.a. scaling), loosing potentially unstable shrubs and bushes, and deploying landslide protection networks. The interested areas are often difficult to reach and maintenance activities are typically performed manually by highly trained human operators. These tasks are challenging and inherently unsafe due to the presence of unstable rocks in the operation area. As it frequently happens, a dangerous human activity in harsh scenarios provides strong motivations for the development of *ad-hoc* robotics solutions, which in our case take the shape of *climbing robots*. A climbing robot is endowed with a package of technical solutions that enable its navigation along difficult and unstable mountain slopes and the execution of complex tasks, such as rock stability assessment, setting anchors in the rock, and scaling loose or dangerous boulders.

Related work. The ability of climbing robots to move on vertical surfaces [1] naturally discloses a wide range of opportunities in application areas such as glass cleaning of tall buildings, pipeline maintenance or infrastructure inspection, such as bridges. In this regard, [2] evaluates various solutions to the problem of automating bridge inspection and maintenance tasks using robotic systems. Compared to the application of flying robots for inspection tasks [3], the use of climbing robots holds the promise of longer mission durations and more accurate operations.

*Corresponding author

Email addresses: michele.focchi@unitn.it (Michele Focchi), andrea.delprete@unitn.it (Andrea Del Prete), daniele.fontanelli@unitn.it (Daniele Fontanelli), marco.frego@unibz.it (Marco Frego), angelika.peer@unibz.it (Angelika Peer), luigi.palopoli@unitn.it (Luigi Palopoli)

A first family of robots in this context are walking climbing robots that are often bio-inspired [4] and have been popular in the last three decades. An example is the Stickybot [5], a gecko-inspired robot with adhesive structure under its toes to hold itself on any kind of surface. Others again took inspiration from the flexible claws of wasps or flies [4]. Such wall-crawling solutions, although fascinating in their design principles, have not made inroads into the market. Their main limitation is the risk of accidental falls, possibly caused by strong wind and/or by the surface condition (e.g., the feet could slip away from the slope in conditions of wet and irregular terrain). The same problems determine strong limits on the payload that these robots can carry.

A different family of solutions is based on hybrid flying/climbing robots, i.e., robots that can fly and that, at the same time can land on, adhere to and ascend vertical surfaces. An example of this kind is Scamp [6], which uses a propeller to stick to the wall. Caros (Climbing Aerial RObot System) [7] is a fairly conventional quadrotor equipped with four wheels and capable of transitioning from the ground to the wall. Its rotors are tilt-controlled, hence their thrust is used to generate aerodynamic adhesion to stick to the wall. The limitation is that the robot can only “slide” on the surface and cannot overcome obstacles. Hybrid propeller-wheeled wall-climbing robots achieve vertical locomotion with wheels by pushing the robot body against the wall using the thrust force of the propellers [8, 9]. Because they can maintain a constant distance to the wall (differently from UAVs), they can capture high quality images of structures for failure/ defect detection. This simplifies the estimation of crack length and width [10]. They can also perform periodic infrastructure health monitoring by performing a hammering test [11]. However, the reduced payload is a strong limitation for the execution of different maintenance tasks.

A third family is given by climbing robots attached to ropes. They are developed for different reasons, ranging from automated cameras hanging over a stadium for dynamic recordings [12], to windows cleaning robots, cranes and other support systems [13, 14], rovers for cave explorations on other planets [15]. The main differences are the positions of the anchor points where the ropes are fixed, which depends on the application. The reachable space of the robot is defined by the number and the position of the attachment points of the cables. Most results involve fixed extrema for all ropes (one or more) [16], and the control is done with non standard optimisation techniques, that combine optimal control or MPC and simplification steps like linearisation, because of the presence of kinematic loops and high nonlinearities in the model. On the other hand, if one end of the ropes is free, the robot will swing and other positioning methods should be envisaged: in fact, the tension is not bilateral. Examples of this family of solution are given by robots hanging on ropes [17, 18, 19] (hanging robots) and are credited with the potential to address the problem of payload limits. In

addition, a robot hanging on ropes can potentially explore large areas, with limited power consumption and with a remarkable speed. An example of a hanging robots with high technology readiness level are BladeBUG [18] and Aerone [19] robots, which can inspect, diagnose, repair, and clean wind turbine blades. Although well engineered, these robots can only operate on surfaces with a regular geometry (e.g., wind turbine blades). Furthermore, they moves with a low speed, due to the crawling motion along the blades. Another example is the Axel/DuAxel robot [20] a rover for space exploration that moves by reeling/unreeling its built-in tether, lowering itself down almost any type of terrain, which has been optimised for resisting to the very cold temperatures of the Moon or Mars and their sand traps. Finally, the aerial robot [21] is a tethered bicopter with horizontal propellers, that by swinging manoeuvres is able to navigate glacial-inspired scenarios, where there are obstacles.

Other hanging robot solutions such as the novel bio-inspired dragline locomotion [22] or CLIO [23], can reach high navigation speed using an actuated winding/releasing mechanism, which is a decisive advantage for applications requiring a prompt intervention over different solutions such as climbing robots that use sticky pads and gaits to climb up/down [24, 25, 26, 27].

An efficient locomotion mechanism is certainly key for a climbing robot. However, other aspects are gaining an equal level of importance. The peculiar nature of the activities required to climbing robots, makes them a difficult fit for full autonomy. Existing solutions require a tight supervision by humans in visual contact from helicopters or special structures, such as telescopic platforms or scaffolds. The difficulty and the costs of this type of human intervention calls for an increased level of autonomy for climbing robots. Two key aspects for increasing autonomy are control and motion planning. Some approaches involved numerical optimisation applied to lower-dimensional template models [28] or hierarchical whole-body controllers to plan the motion of the flying base [29]. In particular, [28] optimises a multi-jump trajectory where the contact locations and the jump time are free variables, thus overcoming a gap obstacle. However, no physical simulation of the approach was provided.

In our previous paper [23], we showed an optimisation of a jump trajectory with a *single* rope. A rope-based climbing robot moving with jumps is somewhat close to the Salto-1P jumping robot [30], but the key feature of jumping with a rope lies in the ability to address terrains of high inclination (up to vertical). In legged robots, jumping motions on the ground are usually synthesised by means of sophisticated numerical optimisation techniques [31, 32]. For example, Ding et al. [33] consider the dynamics up to the actuation level and employ direct optimal control approaches to derive a trajectory for the centre of mass that satisfies constraints and avoids obstacles (e.g. a gap on the wall) and mixed-integer programming approaches in the case that the contact location is not known a pri-

ori. Since the main drawback of these solutions is the exponential computation time, the use of approximations becomes mandatory. As an example, Jiang et al. [34] and Grandia et al. [35] propose using convex polyhedrons to approximate the terrain and constrain the reachability of the robot feet.

Example Use Case and Requirements. The system requirements are best illustrated through a realistic use case related to a typical maintenance operation in a mountainous environment. In this example, the system's objective is to monitor the condition of a steep mountain wall (the slope could be 0.1 radians from the vertical line). Reaching the site is a highly challenging task for humans, requiring advanced mountaineering techniques. Not only are the rock walls steep and difficult to climb, but they are also obstructed by obstacles up to 2 m in size, such as bushes, rock protrusions, and cracks. Replacing humans with a robot necessitates replicating the same navigation capabilities in these harsh conditions.

In the outlined scenario, we assume that the robot has access to a 3D map (e.g., acquired by a drone), but it still requires onboard sensing capabilities to localise itself within the map and to measure its distance from the wall. Moreover, even after reaching the intervention site, the robot must be capable of executing potentially complex operations. For instance, assessing the stability of a boulder might involve hammering and conducting non-destructive testing. Typical equipment for hammering operations [36] is designed to be portable and lightweight, but the duration of such tests can be substantial (in the order of 30 minutes). To function effectively in challenging scenarios such as the one described, the robot must meet the following requirements:

R1 - Carry a payload (e.g., in the order of kilograms) and maintain a stationary position for extended periods without consuming energy (e.g., to perform inspection or maintenance operations such as hammering; see Fig. 1).

R2 - Move quickly and efficiently (e.g., in the order of seconds) with sufficient accuracy (e.g., in the order of centimetres) along very steep, vertical, or slanted mountain slopes.

R3 - Traverse irregular surfaces, overcoming obstacles (e.g., in the order of metres) such as bushes and rock formations.

R4 - Autonomously or semi-autonomously execute a wide range of on-site operations.

Mapping requirements into design choices. The system requirements had a significant influence on the design choices, as detailed below:

- **R1:** ALPINE operates using two ropes, enabling it to carry heavy loads and remain stationary with minimal energy consumption using brakes; the anchor point is designed in such a way that, for the intended motion of the ropes, there is not interference nor friction with other parts of the anchor (e.g. the anchor ring is protruding from the rock).

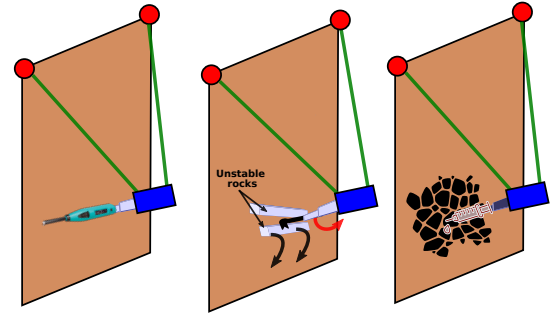


Figure 1: Examples of maintenance operations: hammering (left), debris removal (middle), resin injection (right).

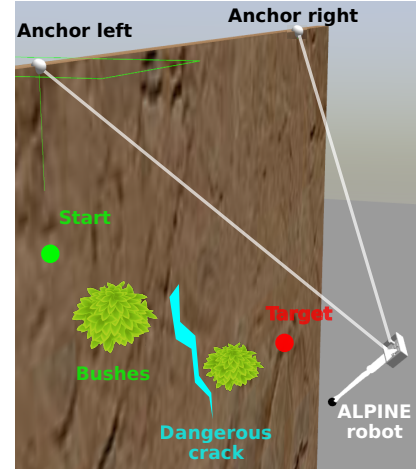


Figure 2: Realistic Gazebo simulation of ALPINE during a jump.

- **R2:** ALPINE coordinates the two ropes and a prismatic leg to quickly push itself away from its resting position for navigation. During jumps and flight, the ropes are independently wound or unwound to control its trajectory, while an auxiliary rotor stabilises the flight. This approach, similarly to the Salto-1p robot [30], demonstrates energy efficiency and high performance in terms of travel time.
- **R3:** The paper presents motion planning and control strategies for navigating while overcoming obstacles (see Figure 2). A simplified model of the system allows for efficient numerical solutions to the multi-jump planning and control problem.
- **R4:** A landing mechanism dissipates the excess of kinetic energy and stabilises the robot on the wall during task execution. Combined with appropriately designed planning and control components, this provides a high degree of operational flexibility.

Scientific challenges. The first scientific challenge of the ALPINE robot lies in its under-actuation: it is impossible to *fully* control the robot's Center of Mass (CoM) when not in contact with the wall. Second, one of the actuators (the leg) operates in an impulsive way, while the ropes can

only operate in the pulling direction (unilateral actuation). The problem is partially alleviated by the auxiliary propeller during the flight phase, but the resulting system dynamics is hybrid (the continuous evolution is interspersed with discrete changes). As regards motion planning, since the motion of the robot depends on both the impulse exerted on the wall and the winding/unwinding of the ropes, a successful strategy should consider the combined effects of under-actuation, rope constraints, the actuator limits and the contact interaction (i.e., friction). Whilst numeric optimisation is certainly a powerful tool [31, 37], the combination of these factors and hybrid dynamics, makes the problem tractability far from obvious.

Paper Contribution and Summary

The contributions of the paper can be summarised as follows.

- The conceptual design of the jumping robot platform ALPINE (Section 2);
- A reduced-order model to simplify the solution of the optimal control strategies (Section 2);
- A static analysis to evaluate the maximum value of operating forces that the system is able to withstand in the execution of its tasks (Section 3);
- A computationally efficient planning algorithm to generate a jump to reach desired targets while overcoming obstacles (Section 4);
- A motion control strategy to track the reference trajectories with high landing accuracy on approximately locally flat surfaces (Section 5).

The efficacy of the system design, as well as of motion planning and control, is tested in a large set of physical simulations (Section 6), while the limits and the future work directions are summarised in Section 7.

Improvements over the preliminary version. The paper builds on a preliminary idea introduced in a conference paper [23] but presents a significant package of innovations that greatly enhance the platform’s effectiveness and operational capabilities. Key advancements include:

- **Enhanced actuation mechanism:** Introducing two ropes and a propeller (instead of one rope) expands the workspace and improves stability during flight.
- **Advanced Control Strategy:** Transitioning to a Model Predictive Controller enables obstacle avoidance and represents a substantial improvement over the original Proportional-Derivative controller paired with a basic motion planning mechanism.
- **Improved landing mechanism:** The new design addresses the limitations of the original retractable leg by incorporating a more realistic and robust landing system.

- **Static equilibrium analysis:** This addition provides a clear evaluation of the device’s operational capabilities.

Extensive simulations validate the realism and practicality of these innovations.

Nomenclature

n	Number of Degrees of Freedom (DoFs) of the system
\mathbf{p}	Position of the robot CoM (reduced-order model)
$\mathbf{p}_{a,i}$	Position of i -th anchor
$\mathbf{p}_{h,i}$	Position of i -th hoist
$\mathbf{p}_{l,i}$	Position of the i -th landing wheel
$\mathbf{J}_{h,i}$	Jacobian of the i -th hoist location
\mathbf{J}_r	Jacobian mapping rope forces/velocities on the CoM
\mathbf{J}_c	Jacobian of the prismatic leg’s foot contact point
\mathbf{M}	Inertia matrix
\mathbf{h}	Bias terms (Centrifugal, Coriolis and Gravity)
$\boldsymbol{\tau}_a$	Actuated generalized forces
μ	Friction coefficient
d_h	Distance of hoist positions on top the base link
d_a	Distance between anchor points
d_b	Distance between landing feet
d_w	Distance of landing feet w.r.t. base frame (along X)
ψ	Reduced-order model state: angle of the ropes w.r.t. to the vertical
l_1	Reduced-order model state: length of the left rope
l_2	Reduced-order model state: length of the right rope
$\mathbf{A}_d, \mathbf{b}_d$	Reduced order model dynamic terms
$\mathbf{A}_p, \mathbf{b}_p$	Polytope constraints matrix
$f_{r,\max / \min}$	Maximum/minimum rope force
$f_{\text{leg},\max}$	Maximum (normal) leg force
\mathbf{n}_\perp	unit vector perpendicular to the rope plane
\mathbf{n}_\parallel	unit vector passing through the anchor points
\mathbf{n}_c	normal of the surface in contact with the prismatic leg’s foot
N	Non Linear Program (NLP) Discretisation steps
N_{mpc}	Model Predictive Control (MPC) Discretisation steps
dt_{sim}	Simulation time interval
dt	Discretisation time interval for the NLP optimisation
dt_{mpc}	Discretisation time interval for the MPC optimisation
t_{th}	Thrust impulse duration
w_s	NLP Smoothing weight

w_{hw}	NLP Hoist work weight
w_i	NLP Impulse work weight
$w_{p/pf/u,mpc}$	MPC weights
δ_i	Impulsive disturbance
δ_c	Constant disturbance
K_L, D_L	Landing strategy impedance parameters
$v_{l,l}, v_{l,r}$	Scalar velocity of the center wheels (parallel to the wall)
$v_{r,l}, v_{r,r}$	Scalar rope speed along the rope axes
R_w	Landing wheels radius
f_{leg}	Leg impulse force
$\mathbf{a}_{r,i}$	i -th rope axis
$f_{r,i}$	i -th rope force
f_p	Propeller force

Unless specified, all vectors are expressed in an inertial frame \mathcal{W} frame (attached to the left anchor). Vectors and matrices are highlighted in bold.

2. Robot Modeling

As mentioned above, a robot hanging on a rope has the ability to preserve energy, when static, by simply engaging the brakes in the hoist. However, a robot hanging on a single rope [23, 28] has severe limitations in terms of possible lateral motions, and hence reachable locations. Additionally, the lateral pull of the rope makes the system unstable when static, limiting its ability to execute tasks. A possible way to tackle these issues is to have an additional prismatic joint (a slider) that enables the motion of the rope anchor point. While easy to control, this solution requires that the slider be mounted on a path clear from obstacles, which is difficult in environments where rock protrusions and bushes are common.

With these limitations in mind, we opted for a different design based on a second rope attached to an additional *fixed* anchor on the wall. Both ropes can be *independently* wound/unwound by means of hoist motors (see Fig. 4). Deploying the two anchors independently removes the limitation of having a clear path for the slider, while the mechanical design is significantly simplified. Another advantage is an increased robustness to disturbances coming from the operations, as detailed in Section 3. The price to pay is a higher control complexity, since the release/winding of the ropes needs to be accurately coordinated.

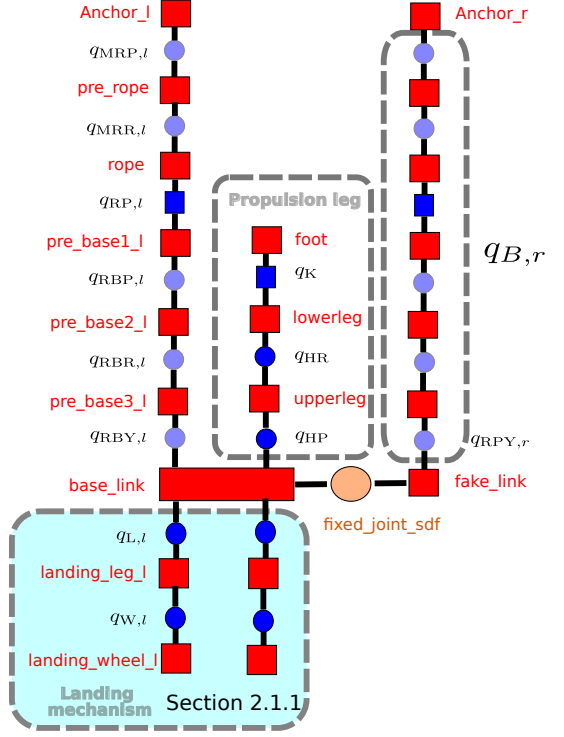


Figure 3: Topology of the joints for the full detail model. Links are red boxes and joints blue circles (revolute) or blue boxes (prismatic). Shaded joints are the passive ones, not shaded ones are the active ones.

2.1. Full robot model

We model the robot as 3 kinematic chains branching from the base link (see Fig. 3). One chain represents the propulsion mechanism (a 3-DoF prismatic leg) [23]: at the extreme of the leg there is a point-like foot. The leg is also endowed with two *adjacent* rotational joints, called hip pitch (q_{HP} , rotating about the base Y axis) and hip roll (q_{HR} , rotating about the base X axis). These joints are needed to align the leg to the *thrusting* impulsive force. A prismatic knee joint (q_K) is used to generate the *thrusting* impulsive force. The landing mechanism is represented by two additional rotational joints that move the landing links (see Fig. 5) with two passive wheels at the extreme as described in more detail in Section 2.1.1.

The other two kinematic chains model the two ropes. To host the hoist motors, the attachment points of the ropes are mounted with an offset $d_h/2$ w.r.t. the base frame (see Fig. 4). We model the attachment between each anchor and the corresponding rope by 2 *passive* (rotational) joints. Each rope can be seen as an *actuated* prismatic joint ($q_{RP,l}$ or $q_{RP,r}$), followed by 3 *passive* rotational joints to model the connection between the rope and the *base link*. The described mounting choice is indeed equivalent to allocating 3 joints at the anchor point and 2 at the base. However, to avoid a redundant representation, there must be only one passive rotational joint

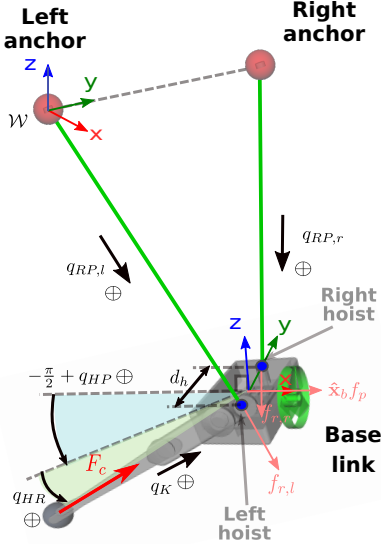


Figure 4: Kinematic model of the ALPINE robot with two ropes (standard definitions). A propeller is mounted on the rear of the robot. In pink are depicted all the actuation forces. The inertial (\mathcal{W}) frame is attached to the left anchor frame.

aligned with the rope. To increase the robot controllability (e.g. capability to apply forces on the base) along the direction perpendicular to the ropes plane, we added a propeller mounted on the back of the base link, as depicted in Fig. 4. This brings several advantages. 1) It allows the robot to reject disturbances and reduce tracking errors (during the flight) in the direction perpendicular to the ropes plane, enhancing controllability. 2) It increases the maximum force the robot can withstand during operations without losing contact. This is particularly relevant when dealing with harder rocks: by activating the propellers to provide additional push against the walls, we can increase the force margin available for more demanding operations, such as drilling. 3) It enables the control of the robot orientation both in contact and 4) during the flight, by actuating the propellers in a differential way. In this paper, we will focus on exploiting only the disturbance rejection feature 1), and the reorientation 3) leaving the other two features for future works. Theoretically, the propeller itself could be used in place of the prismatic leg to generate the push from the wall. However, the explosive motion required to achieve high acceleration in a short time interval is difficult to achieve with a propeller. Therefore, we chose to rely on a prismatic actuator specifically designed for this purpose. In this design, we preferred to keep the propeller size contained and use it only for corrections of the deviations from the desired trajectory due to environmental disturbances (see Section 5.1). The differential commanding of a couple of propellers could enable the horizontal alignment of the leg to the *thrusting* impulse, removing the need for the q_{HR} joint. We showcase in the accompanying video the solutions with both q_{HR} and q_{HP} joints and with propellers plus q_{HP} joint.

Neglecting the 4 joints of the landing mechanism (see

Section 2.1.1) and the propeller, the total number of DoFs is $n = 15$, represented by the configuration vector $\mathbf{q} \in \mathbb{R}^{15}$. Ten of these joints are relative to the attachment of the ropes to the hoist and the anchor and are passive. Fig. 3 illustrates the joint definitions: *MRX* (Mountain Rope X = Pitch/Roll), *RP* (Rope Prismatic) and *RBX* (Rope Base X = Roll/Pitch/Yaw). By stacking the different joint variables related to the left rope, we obtain the vector $\mathbf{q}_{B,l} = [q_{MRP} \ q_{MRR} \ q_{RP} \ q_{RBP} \ q_{RBR} \ q_{RBY}]^T$. We can repeat the same for the right rope stacking the joint variable into the vector $\mathbf{q}_{B,r}$ and come up with the definition of the joint state $\mathbf{q} = [\mathbf{q}_{B,l}^T \ \mathbf{q}_{B,r}^T \ q_{HP} \ q_{HR} \ q_K]^T$, where additionally we have *HX* (Hip X = roll/pitch) and *K* (Knee) joints. The dynamic equation of motion is subject to a holonomic constraint because the two attachment points $\mathbf{p}_{h,l}(\mathbf{q})$, $\mathbf{p}_{h,r}(\mathbf{q})$ should maintain a fixed distance d_h among them, i.e.

$$\|\mathbf{p}_{h,l}(\mathbf{q}) - \mathbf{p}_{h,r}(\mathbf{q})\|^2 = d_h^2. \quad (1)$$

This description creates a kinematic loop represented by the trapezoid having the two ropes as edges. The full dynamic equation is reported here just for reference

$$\left\{ \begin{array}{l} \mathbf{M}(\mathbf{q})\ddot{\mathbf{q}} + \mathbf{h}(\mathbf{q}, \dot{\mathbf{q}}) = \begin{bmatrix} \mathbf{0}_{10 \times 1} \\ \tau_a \end{bmatrix} + \mathbf{J}_c(\mathbf{q})^T \mathbf{f}_c + \mathbf{J}_p(\mathbf{q})^T f_p, \\ \mathbf{A}(\mathbf{q})\dot{\mathbf{q}} = \mathbf{0}, \\ \tau_{RP,l} \geq 0, \\ \tau_{RP,r} \geq 0, \end{array} \right. \quad (2)$$

where $\mathbf{M} \in \mathbb{R}^{n \times n}$ is the inertia matrix, $\mathbf{h} \in \mathbb{R}^n$ represents the bias terms (Centrifugal, Coriolis and Gravity), and $\mathbf{J}_c \in \mathbb{R}^{3 \times n}$ is the Jacobian relative to the prismatic leg contact point (foot) that maps the contact force $\mathbf{f}_c \in \mathbb{R}^3$ into the generalised coordinate space. $f_p \in \mathbb{R}$ is a scalar and represents the magnitude of the propeller force that is mapped into the robot dynamics through the transpose of $\mathbf{J}_p(\mathbf{q}) = \hat{\mathbf{x}}_b^T \mathbf{J}_b(\mathbf{q}) \in \mathbb{R}^{1 \times n}$, where $\hat{\mathbf{x}}_b$ is the X axis of the base link and $\mathbf{J}_b(\mathbf{q}) = \left[\frac{\partial \mathbf{p}(\mathbf{q})}{\partial \mathbf{q}} \right] \in \mathbb{R}^{3 \times n}$ is the Jacobian of the robot base. The $\mathbf{A}(\mathbf{q})\dot{\mathbf{q}} = \mathbf{0}$ constraint is (1) rewritten at the velocity level. The force/torque variable of the the actuated joints are grouped into the vector $\tau_a = [\tau_{RP,l} \ \tau_{RP,r} \ \tau_{leg}]^T \in \mathbb{R}^5$. We will employ the right hand side of (2) to express the mapping of the contact force and of the propeller force into joint torques.

2.1.1. Landing Mechanism

The robot in Fig. 4 would not be able to self-stabilise on the wall with a single leg, therefore we designed a *landing* mechanism, depicted in Fig. 5, formed by two additional rotational joints $q_{L,l}$ and $q_{L,r}$ located on the sides of the base link allowing to activate two landing legs. Moreover, we added two wheels at the tips of the landing legs, which can move *laterally* during the contact and, hence, avoid the generation of *internal* forces (i.e., parallel to the wall).

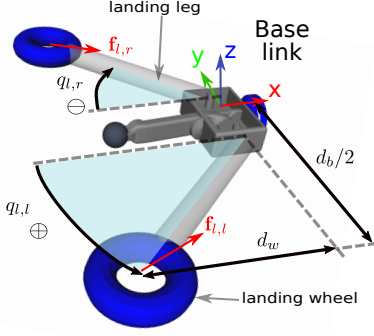


Figure 5: Overview of the landing mechanism, with joint and variable definitions. d_w and d_b are the wall clearance and distance between landing wheels. Passive wheels are attached to the extremes of the landing legs.

2.2. Reduced-order model with minimal representation

The high number of states and the constraint in (2) makes the full dynamics hardly tractable for control design. For this reason, we derive a lower dimensional (reduced-order) model with only 3 DoFs that captures the dominant dynamics of the system along with the holonomic kinematic constraint (1). To this end, we make the following simplifying assumptions: 1) the mass is entirely concentrated in the body attached to the rope and we neglect the angular dynamics and 2) during the winding/rewinding of the ropes they remain completely tight (i.e., they are not bending).

In order to simplify the control design, we approximate the rope attachment points as coincident and then choose a *minimal* representation for the state with 3 DoFs. Specifically, the reduced state \mathbf{q}_r is defined as $\mathbf{q}_r = [\psi \ l_1 \ l_2] \in \mathbb{R}^3$, where ψ is the angle formed from the ropes plane and the wall, and l_1, l_2 the length of the left and right ropes, respectively. A geometric scheme of the reduced model with vector definitions is shown in Fig. 6. Assuming the inertial frame \mathcal{W} attached to the *left* anchor point, the dynamics of the point \mathbf{p} (where the robot mass is concentrated, by assumption) is defined by the Newton Equation:

$$m(\ddot{\mathbf{p}} - \mathbf{g}) = \underbrace{\hat{\mathbf{a}}_{r,l} f_{r,l}}_{\mathbf{f}_{r,l}} + \underbrace{\hat{\mathbf{a}}_{r,r} f_{r,r}}_{\mathbf{f}_{r,r}} + \mathbf{f}_{leg} + \hat{\mathbf{x}}_b f_p, \quad (3)$$

where $\hat{\mathbf{a}}_{r,i} = \frac{\mathbf{p} - \mathbf{p}_{a,i}}{\|\mathbf{p} - \mathbf{p}_{a,i}\|} \in \mathbb{R}^3$ and $f_{r,i} \in \mathbb{R}$, with $i = \{r, l\}$, are the rope axes and the magnitude of the exerted forces, respectively. The term $\hat{\mathbf{x}}_b f_p$ represents the propeller's force where $\hat{\mathbf{x}}_b \in \mathbb{R}^3$ is the base link X unit axis which is perpendicular to the ropes' plane.¹

The two anchor point positions are given by $\mathbf{p}_{a,l}$ and $\mathbf{p}_{a,r}$. The input variables are: 1) the rope forces $\mathbf{f}_{r,i}$ oriented along the rope axes; 2) an impulsive pushing force

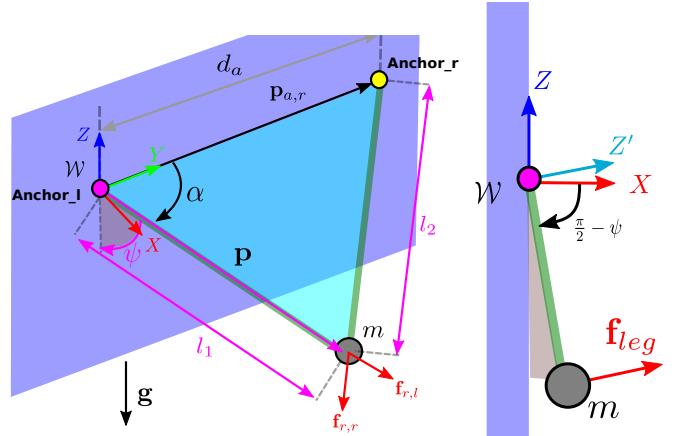


Figure 6: Reduced order model with two anchor points: standard definitions (left) and side view (right). The impulsive force \mathbf{f}_{leg} is applied only when the leg is in contact.

\mathbf{f}_{leg} (applied at \mathbf{p}) that the robot generates when in contact with the mountain (see Fig. 6). Therefore, the expression of the forward kinematics for the position \mathbf{p} of the robot (origin of the base-link) as a function of \mathbf{q}_r is given by:

$$\mathbf{p}(\mathbf{q}_r) = \begin{bmatrix} l_1 \sin(\psi) \sqrt{1 - \frac{(d_a^2 + l_1^2 - l_2^2)^2}{4d_a^2 l_1^2}} \\ (d_a^2 + l_1^2 - l_2^2)/(2d_a) \\ -l_1 \cos(\psi) \sqrt{1 - \frac{(d_a^2 + l_1^2 - l_2^2)^2}{4d_a^2 l_1^2}} \end{bmatrix}, \quad (4)$$

where the holonomic constraint (1) has been embedded (by construction) thanks to specific choice of coordinates \mathbf{q}_r and d_a is the distance between the anchors. The dynamics of the point mass as defined in (3) is given by the second derivative of (4), which gives an implicit expression for the coupled derivatives $\dot{\psi}, \ddot{l}_1$ and \ddot{l}_2 , thus leading to the following matrix form of (3)

$$m \underbrace{\left(\mathbf{A}_d \begin{bmatrix} \ddot{\psi} \\ \ddot{l}_1 \\ \ddot{l}_2 \end{bmatrix} + \mathbf{b}_d \right)}_{\ddot{\mathbf{p}}} = \underbrace{m\mathbf{g} + \mathbf{f}_{leg} + \mathbf{J}_r \begin{bmatrix} f_{r,l} \\ f_{r,r} \end{bmatrix} + \hat{\mathbf{x}}_b f_p}_{\mathbf{f}_{tot}}, \quad (5)$$

where \mathbf{A}_d and \mathbf{b}_d are reported in the Appendix, and $\mathbf{J}_r = [\hat{\mathbf{a}}_{r,l} \ \hat{\mathbf{a}}_{r,r}] \in \mathbb{R}^{3 \times 2}$. Finally, we obtain:

$$\begin{bmatrix} \ddot{\psi} \\ \ddot{l}_1 \\ \ddot{l}_2 \end{bmatrix} = \mathbf{A}_d^{-1} \begin{bmatrix} 1 \\ m \mathbf{f}_{tot} - \mathbf{b}_d \end{bmatrix}. \quad (6)$$

Note that this model has a singularity when the term $\sin(\psi)$ in \mathbf{A}_d becomes zero. The configuration $\psi = 0$ corresponds to the robot base lying on the vertical wall, which never happens if the ropes are connected directly (i.e., without obstacles in between) to the robot base, due to the presence of the leg. For over-hanging walls, no rope-based system can be employed because the contact cannot be ensured nor maintained.

¹Differently from (2), because we adopt a point mass assumption, the base link is always aligned with the ropes' plane (i.e. $\mathbf{n}_\perp = \hat{\mathbf{x}}_b$).

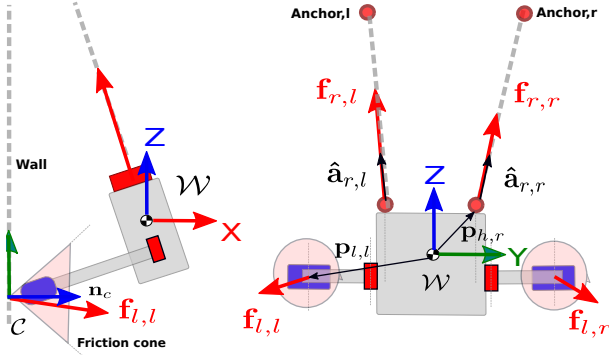


Figure 7: Definition of vectors and frames for the rigid body model used in the static analysis: (left) side view (right) front view. Differently from Section 2, the inertial frame W is attached to the CoM.

3. Static Analysis

3.1. Feasible Polytope

In this section we present a numerical procedure to evaluate the *static* stability of the robot for a set of locations once landed on the wall. Since the robot with only one leg would be inherently unstable on the wall, we consider the ensemble robot *and* landing mechanism. The analysis aims to answer the following queries: **(Q1)** Is it possible to find a static balance between gravity, rope tensions and forces at the landing wheels for a given position that allows the robot to remain in contact with the wall? The presence of this equilibrium is key to the execution of any robot task. **(Q2)** How do the limits on the actuators and the presence of external forces affect static stability? More generally, for each robot location on the wall it is important to evaluate the maximum operation forces that can be generated. Both aspects are fundamental to execute any task, since the contact forces generated for maintenance operation (called operation forces) must be balanced by the landing wheels and by the ropes. For instance, if operation forces required a force on the feet violating the unilateral condition, the robot will tip over. To answer **Q2** we consider unilaterality, friction and *actuation* constraints, while to answer **Q1** only unilaterality and friction are sufficient.

The following assumptions underlie the present analysis: 1) we approximate the assembly robot+landing mechanism as a *rigid body* which is in contact with the wall with the *landing wheels*; 2) we neglect the masses of the legs of the landing mechanism; 3) we assume that the contact forces for the landing wheels are linear forces (i.e. point contacts) limited by the *unilateral* and *friction cone* constraints. For this analysis we introduce the concept of Feasible Wrench Polytope (FWP) [38] and we refer to Fig. 7 for standard definitions.

The FWP represents the set of *feasible* wrenches at the centroid (i.e., forces and moments) than can be tolerated while satisfying 1) the balance equation of forces under the action of gravity (static condition), 2) unilateral conditions of the contacts, 3) friction constraints and 4) actuation

limits. Therefore, the feasible wrenches can be seen as a compact representation of the mentioned constraints 1-4 projected at the CoM by means of a Minkowski sum operation.

Proceeding with the computation of the FWP [38], the first step is to compute the Force polytopes \mathcal{F}_i associated with the feet and rope forces. We define 4 unilateral contacts, two at the *landing wheels* and two at the rope attachment points with the base (refer to Fig. 7). In the case of the landing wheels, friction constraints are present while the ropes have an additional constraint on the direction: namely, the force has to be acting along the rope axis. Adopting an approximation that is commonplace in robotics, we (conservatively) approximate the cone constraint with an inner pyramid and bound them along the normal direction with the maximum $f_{\text{leg},\text{max}}$. Note that the friction cone implicitly encodes also the unilateral constraint ($\mathbf{n}_c^T \mathbf{f}_{l,i} > 0$). This way, we encode in a single matrix of constraints: unilateral, friction and actuation bound for the i -th wheel. The vertices of the obtained force polytope are stored as columns:

$$\mathbf{f}_{l,i}^{\text{lim}} = \mathcal{W} \mathbf{R}_c(\mathbf{n}_c) \begin{bmatrix} 0 & \mu & -\mu & -\mu & \mu \\ 0 & \mu & \mu & -\mu & -\mu \\ 0 & 1 & 1 & 1 & 1 \end{bmatrix} f_{\text{leg},\text{max}}, i \in \{l, r\}, \quad (7)$$

where $\mathcal{W} \mathbf{R}_c$ is the rotation matrix related to the contact frame C and $f_{\text{leg},\text{max}}$ is the maximum force in the normal direction \mathbf{n}_c . Regarding the rope forces, they are constrained to lie on a mono-dimensional manifold (i.e. along the axis $\hat{\mathbf{a}}_{r,i}$) and subject to unilateral ($f_{r,i} < 0$) and actuation constraints ($-f_{r,i}^{\text{max}} \leq f_{r,i} \leq f_{r,i}$). Then the Force Polytope associated to rope i boils down to a segment with only two vertices:

$$\mathbf{f}_{r,i}^{\text{lim}} = [-\hat{\mathbf{a}}_{r,i} \quad \mathbf{0}_{3 \times 1}] f_{r,\text{max}}, i \in \{l, r\}, \quad (8)$$

Next, for each vertex, we add the moments that are generated in correspondence to the maximum forces:

$$\mathbf{w}_{l,i} = \begin{bmatrix} \dots \mathbf{f}_{l,i,k}^{\text{lim}} \dots \\ \dots \mathbf{p}_{l,i} \times \mathbf{f}_{l,i,k}^{\text{lim}} \dots \end{bmatrix} \quad \text{with } k = 1, \dots, 5, \quad (9)$$

where $\mathbf{p}_{l,i} \in \mathbb{R}^3$ represents the position of the i -th landing wheel and $\mathbf{w}_{l,i,k} \in \mathbb{R}^6$ represents a wrench that can be realised at that wheel. Likewise, for ropes:

$$\mathbf{w}_{r,i} = \begin{bmatrix} -\hat{\mathbf{a}}_{r,i} & \mathbf{0}_{3 \times 1} \\ -\mathbf{p}_{h,i} \times \hat{\mathbf{a}}_{r,i} & \mathbf{0}_{3 \times 1} \end{bmatrix} f_{r,\text{max}}, \quad (10)$$

where $\mathbf{p}_{h,i} \in \mathbb{R}^3$ is the i -th rope attachment point. Therefore, the set of admissible wrenches that can be applied at the CoM by the i -th wheel is:

$$\mathcal{W}_{l,i} = \text{ConvexHull}(\mathbf{w}_{l,i,1}, \dots, \mathbf{w}_{l,i,5}), \quad i \in \{l, r\}. \quad (11)$$

The convex hull operation should be performed also for ropes to compute $\mathcal{W}_{r,i}$ and has the purpose to eliminate internal vertices. We now have 4 wrench polytopes \mathcal{W}_i that

contain all the admissible wrenches that can be applied to the robot's CoM.

Finally, the FWP is computed through the Minkowski sum of the \mathcal{W}_i for all the contacts:

$$FWP = \bigoplus_{i=1}^4 \mathcal{W}_i. \quad (12)$$

Since we used a vertex description (\mathcal{V} -description), the Minkowski sum can be efficiently obtained as in [39]. **Remark:** To avoid polytopes becoming flat² it is preferable to define all quantities w.r.t. an inertial frame placed in a location different from the anchors. More precisely, it is convenient to refer all quantities about the CoM (see Fig. 7). Henceforth, **only for this section**, we assume that the inertial frame is attached to the CoM and not to the left anchor. In a preliminary analysis, to answer **Q1**, we assume there are no actuation limits. The FWP, in this case becomes unbounded, and becomes a Contact Wrench Cone (CWC) [40]. We define a robot position *feasible* if there exists a set of rope and wheel forces that 1) ensures static equilibrium, 2) ensures unilateral and friction constraints.

3.2. Gravitational wrench

To evaluate the feasibility of a robot location, we first compute the gravito-inertial wrench \mathbf{w}_G in the specific robot state. Because we are dealing with a static analysis we neglect the inertial effects:

$$\mathbf{w}_G = \begin{bmatrix} mg \\ \mathbf{p} \times mg \end{bmatrix}, \quad (13)$$

where \mathbf{p} is the robot CoM position (equal to $\mathbf{0}$ because the inertial frame is attached to the CoM). A *feasibility criterion* can be written as:

$$\mathbf{w}_G \in FWP. \quad (14)$$

The criterion (14) tells us that it exists a feasible set of forces $[(\hat{\mathbf{a}}_{r,l} f_{r,l}), (\hat{\mathbf{a}}_{r,r} f_{r,r}), \mathbf{f}_{l,l}, \mathbf{f}_{l,r}]$ that generates the wrench \mathbf{w}_G . We evaluate (14) at different positions on the wall, on a fine grid. We set a friction coefficient of $\mu = 0.8$, a distance of the anchors $d_a = 5$ m, the relative distance of the landing wheels $d_b = 0.8$ m and the wall clearance $d_w = 0.4$ m (see Fig. 5). The outcome of this analysis is that the set of equilibrium locations on the wall is mostly limited to the rectangle delimited by two anchors (red shaded area \mathcal{A} in Fig. 8).

To answer **Q2**, we are interested in the *additional* operation forces that can be tolerated when the robot is in *equilibrium*, for which we want to evaluate the operating margin. This time, we also consider *actuation* limits, and find that the answer is closely correlated to the concept of *feasibility margin*, which can be computed from the FWP.

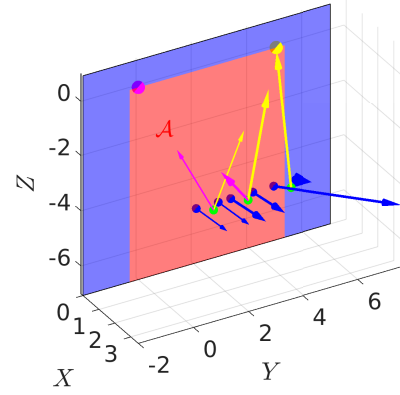


Figure 8: Results of the static analysis in three representative points for $\mathbf{p}_z = 5$ m. The red shaded area \mathcal{A} indicates all the robot positions for which static equilibrium, unilateral and friction constraints are fulfilled. We report the forces for 3 representative robot positions. The figure shows that, the rope connected to the closer anchor point gets gradually loaded when moving towards it, while the rope connected to the farther anchor gets gradually unloaded.

We recall that the FWP represents the set of admissible centroidal wrenches for a specific position of the robot on the wall, where: 1) centroidal it means applied at the CoM, 2) admissible it means that this is a "mapping" of contact forces satisfy both friction and unilateral constraints at the landing legs and ropes have tensions such that do not get unloaded or exceed their limits. When the wrench goes out of the FWP it means that one of the above constraints is violated (e.g. one leg slips or it becomes unloaded, and the robot tips over).

The feasibility margin of applicable operating forces is defined as the smallest distance between the gravitational wrench \mathbf{w}_G and the boundaries represented by the FWP facets. Authors in [38] show that an estimate of this margin could be obtained directly from the vertex (\mathcal{V}) description. However, a margin computed with the vertex description is a normalised value. Additionally, we might be interested in evaluating the maximum wrench and then the relative margin in a *specific* direction $\hat{\mathbf{v}} \in \mathbb{R}^6$. In this case the vertex description is no longer sufficient, and we ought to derive the half-plane (i.e. \mathcal{H} -description) of the FWP from the \mathcal{V} -description via the *double description* algorithm [41]. In the \mathcal{H} -description, the FWP set can be written in terms of half-spaces as:

$$FWP = \{\mathbf{w} \in \mathbb{R}^6 | \hat{\mathbf{a}}_j^T \mathbf{w} \leq 0, j = 1, \dots, n_h\}, \quad (15)$$

where n_h is the number of half-spaces of the FWP and $\hat{\mathbf{a}}_j \in \mathbb{R}^6$ is the normal vector to the j -th facet. The feasibility criterion expressed in (14) can thus be formulated as:

$$\mathbf{A}_p \mathbf{w}_G \leq \mathbf{b}_p, \quad (16)$$

where $\mathbf{A}_p \in \mathbb{R}^{n_h \times 6}$ is the matrix whose rows are $\hat{\mathbf{a}}_j$.

3.3. Evaluating the feasibility margin

The feasibility margin $\gamma \in \mathbb{R}$ in the direction $\hat{\mathbf{v}}$ is the distance (along $\hat{\mathbf{v}}$) between \mathbf{w}_G and the polytope bound-

²A flat polytope is a polytope that has some vertex lying on its facets.

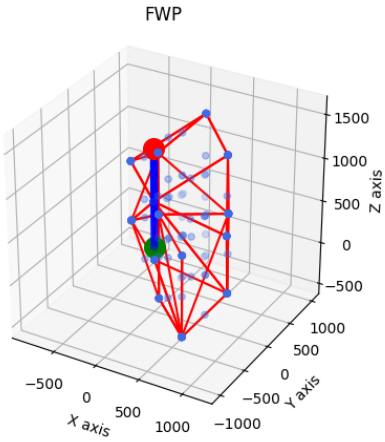


Figure 9: Representation of the linear part of the FWP computed for a position $\mathbf{p} = [1.5, 2.5, -6.5]^T$. The green point is the gravitational force $\mathbf{w}_{G,lin}$. The red point is the maximum force along the direction $\hat{\mathbf{v}} = [0, 0, 1, 0, 0, 0]$ (blue line). Shaded blue points are internal points that are removed by the convex hull operation.

ary and can be obtained by solving the following Linear Program (LP):

$$\gamma^* = \operatorname{argmin}_{\gamma} -\gamma \quad (17a)$$

$$\text{s.t. } \mathbf{A}_p(\mathbf{w}_G + \gamma\hat{\mathbf{v}}) \leq \mathbf{b}_p, \quad (17b)$$

Hereby, (17b) ensures that the total wrench $\mathbf{w}_G + \gamma\hat{\mathbf{v}}$ is inside the FWP set. The solution γ^* of (17) gives the surplus of additional external wrench $\gamma^*\hat{\mathbf{v}}$ that can be tolerated by the system [38]. Since it is not possible to visually represent a set of 6D elements using a 3D figure, in Fig. 9, we depict only the linear component of the FWP (i.e., the set of admissible *centroidal* linear forces), computed for the position $\mathbf{p} = [1.5 \ 2.5 \ -6.5]^T$. In this representation, the green dot indicates the gravitational force, while the red dot shows the maximum additional force that can be applied in the direction of the blue line (oriented vertically) before becoming unfeasible.

3.4. Numeric evaluation

In a first representative operation, that ensembles a hammering operation, we compute the feasibility margin to generate a pure force (i.e. passing through the CoM) along the X direction $\hat{\mathbf{v}} = [-1 \ 0 \ 0 \ 0 \ 0 \ 0]^T$ for robot positions with Y ranging between the two anchors (i.e. from 0 to 5 m) and the Z component ranging from -2 to -10 m. We repeat the analysis for two different wall inclinations (0.2 and 0.4 rad) that will result in different \mathbf{n}_c . To have the robot in contact, the X component is set to 1.7 and 3 m, respectively. Figure 10 (left plots) reports the 2D (heat-map) representation of the value of the feasibility margin for the two different wall inclinations. The friction coefficient is set to $\mu = 0.8$. As expected, the mar-

gin decreases with the distance to the anchors because the angle ψ decreases with rope elongation (for the same wall clearance), and pushing on the wall becomes more difficult because the legs get more and more unloaded. For the same reason, a more slanted wall involves overall higher gravity components and, hence, overall more feet loading, thus higher values for the margin can be observed. The diagonal shape is related to the friction constraint which is violated in the dark blue area. In these cases the whole static feasibility is invalidated (i.e. \mathbf{w}_G goes out of the polytope) and we set the margin to be null.

In a second analysis (see Fig. 10, right plots) we consider a *composite* loading as observed in a *debris removal* application, pictorially represented in Fig. 1, middle. This time we consider a purely vertical wall (i.e. $\mathbf{n}_c = [1 \ 0 \ 0]^T$) with a constant $\mathbf{p}_x = 1.5$ m. Interestingly, for the margin in the vertical direction, only two values are possible: zero in the region for which friction constraints are violated (we did a parametric analysis for $\mu = \{0.4, 0.6, 0.8\}$ to highlight its influence), and the value of the gravity (147 N) in the remaining region. This means that the vertical push is obtained through the action of gravity and cannot go beyond that. We also noticed that the position of the feet is fundamental to achieve a stable configuration (i.e. they cannot be shifted too much w.r.t the CoM in the vertical direction, cf. Fig 7). The results for the moment \mathbf{m}_y (fourth plot) are more inline with the \mathbf{f}_x case, where higher margins are related to positions between the anchors. This is a *quantitative* evaluation that is important for real operations: being able to evaluate the operating margin is a feature useful to optimise costs-related maintenance operations depending on the type of the rock. Being able to estimate the maximum force applicable gives benefits in terms of cost effectiveness, because it allows to minimise the time budget for the operation.

4. Motion Planning

Setting up a navigation approach for the ALPINE robot is a non-trivial task. First of all, even the simplified dynamics (6) is highly nonlinear. Second, the configurations between which the robot moves are usually distant, and therefore, linearising the dynamics around an operating point would lead to inaccurate results. Third, one of the inputs, the thrusting force \mathbf{f}_{leg} , has an impulsive nature, operating at discrete time instants, and its tangential component is constrained by friction. Therefore, it is not possible to use it in any feedback control scheme.

As customary in robotics, we split the navigation problem into two sub-problems: 1) motion planning, i.e., deciding a trajectory before the motion starts, 2) motion control, i.e., a feedback controller that operates the rope/propeller forces to compensate for small deviations to track the trajectory and land in proximity of the expected position. This section focuses on step 1 and considers the robot *without* the landing mechanism. The motion plan

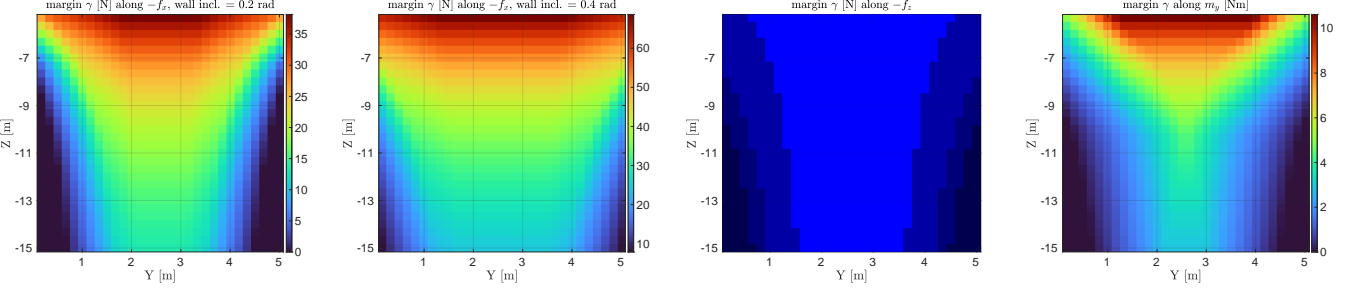


Figure 10: Heat-maps of the feasibility margin computed for different positions along the wall, (left plots) along $-\mathbf{f}_x = [-1, 0, 0, 0, 0, 0]^T$ for a hammering application, for a wall inclination of 0.2 rad (first), and 0.4 rad (second) and (right plots) along $-\mathbf{f}_z = [0, 0, -1, 0, 0, 0]^T$ (third) and $\mathbf{m}_y = [0, 0, 0, 0, -1, 0]^T$ direction (fourth) relative to a debris removal operation which involves the application of a not purely centroidal force (also a moment). In the third plot we reported the results for 3 values of the friction coefficient $\mu = \{0.4, 0.6, 0.8\}$. The feasibility margin is a synthetic metric to estimate the amount of external forces and moments available for operations. We report the absolute value of the margin γ .

for the robot is decided by solving a *nonlinear* optimal control problem (OCP), which in general is modelled as follows:

$$\min_{\mathbf{x}(t), \mathbf{u}(t)} m_f(\mathbf{x}(t_f)) + \int_0^{t_f} l(\mathbf{x}(t), \mathbf{u}(t)) dt, \quad (18a)$$

s.t.

$$\dot{\mathbf{x}}(t) = \mathbf{f}(\mathbf{x}(t), \mathbf{u}(t)), \quad (18b)$$

$$\mathbf{u}(t) \in \mathcal{U}, \quad (18c)$$

$$\mathbf{h}(\mathbf{x}(t), \mathbf{u}(t)) \leq 0, \quad (18d)$$

$$\mathbf{B}(\mathbf{x}(t_0), \mathbf{x}(t_f)) = 0, \quad (18e)$$

where $l(\mathbf{x}, \mathbf{u})$ and $m_f(\mathbf{x})$ are the running and the terminal costs, \mathbf{x} is state, \mathbf{U} is the control input constrained in the convex set \mathcal{U} , \mathbf{f} is the dynamics, \mathbf{h} are the *path* constraints, and \mathbf{B} are the boundary conditions. To reduce the computational effort, we consider as \mathbf{f} the reduced-order model (6), which implicitly includes the closed-loop kinematic constraints. The control inputs should include both the rope forces $\mathbf{u} = [f_{r,l}, f_{r,r}] \in \mathbb{R}^2$ and the leg impulse. However, the latter is applied only during the thrusting phase, which typically lasts a short amount of time $t_{th} \in \mathbb{R}$. For this reason, we assume it remains constant during this phase, and treat it as an additional *state* with null dynamics. As decision variables, we consider: 1) the vector of control inputs $\mathbf{U} = [\mathbf{F}_{r,l}, \mathbf{F}_{r,r}]$ where $\mathbf{F}_{r,l}, \mathbf{F}_{r,r}$ are the trajectories of the rope forces along the horizon, 2) the horizon length $t_f \in \mathbb{R}$, and 3) the initial leg impulse $\mathbf{f}_{leg} \in \mathbb{R}^3$.

System Dynamics. Because we define *a priori* the duration of the thrusting phase, the dynamics of our system is no longer hybrid but *time-varying*. When the leg is in contact, the dynamics accounts for the force $\mathbf{f}_{leg}(t)$ generated by the thrusting leg. Rather than modelling this force as an impulse, we model it as:

$$\mathbf{f}_{leg}(t) = \begin{cases} \mathbf{f}_{leg} & 0 \leq t \leq t_{th}, \\ \mathbf{0}_{3 \times 1} & t > t_{th}. \end{cases} \quad (19)$$

Hence, during the contact $t \in [0, t_{th}]$, the leg applies a constant force \mathbf{f}_{leg} while, for $t \in [t_{th}, t_f]$, this force is

zero. Given the nature of our actuation mechanism, a realistic choice is to have a duration in the order of tens of milliseconds, which consequently determines a remarkable intensity of the impulse. We incorporate the leg force $\mathbf{f}_{leg}(t)$ in the state vector \mathbf{x} with a null dynamics. The state of our problem, hence, is defined as:

$$\mathbf{x} = [\psi \quad l_1 \quad l_2 \quad \dot{\psi} \quad \dot{l}_1 \quad \dot{l}_2 \quad \mathbf{f}_{leg}^T]^T \in \mathbb{R}^9. \quad (20)$$

However, when the contact is broken at $t = t_{th}$, the variable \mathbf{f}_{leg} must disappear from the state. We model this change in state dimension by defining a matrix \mathbf{S} that selects the first 6 elements of the 9D state vector:

$$\mathbf{x}^+ = \mathbf{S} \mathbf{x}, \quad t = t_{th}, \quad (21)$$

Consequently, the *state-space* representation of the nonlinear dynamics, casted in input-affine form, can be derived from (6):

$$\begin{aligned} \dot{\mathbf{x}} &= \mathbf{f}_{leg}(\mathbf{x}) + \mathbf{g}_{leg}(\mathbf{x})\mathbf{u}, & t < t_{th}, \\ \dot{\mathbf{x}} &= \mathbf{f}_{noleg}(\mathbf{x}) + \mathbf{g}_{noleg}(\mathbf{x})\mathbf{u}, & t > t_{th}, \end{aligned} \quad (22)$$

where:

$$\mathbf{f}_{leg}(\mathbf{x}) = \begin{bmatrix} \mathbf{x}_{4 \dots 6} \\ \mathbf{A}_d^{-1} \left[\frac{\mathbf{x}_{7 \dots 9}}{m} + \mathbf{g} - \mathbf{b}_d \right] \\ \mathbf{0}_{3 \times 1} \end{bmatrix} \quad (23)$$

$$\mathbf{g}_{leg}(\mathbf{x}) = \begin{bmatrix} \mathbf{g}_{noleg}(\mathbf{x}) \\ \mathbf{0}_{3 \times 2} \end{bmatrix} \quad (24)$$

$$\mathbf{f}_{noleg}(\mathbf{x}) = \begin{bmatrix} \mathbf{x}_{4 \dots 6} \\ \mathbf{A}_d^{-1}(\mathbf{g} - \mathbf{b}_d) \end{bmatrix} \quad (25)$$

$$\mathbf{g}_{noleg}(\mathbf{x}) = \begin{bmatrix} \mathbf{0}_{3 \times 1} & \mathbf{0}_{3 \times 1} \\ \mathbf{A}_d^{-1} \dot{\mathbf{a}}_{r,l} & \mathbf{A}_d^{-1} \dot{\mathbf{a}}_{r,r} \end{bmatrix} \quad (26)$$

To solve OCP (18) we apply a *direct method* to transform the infinite dimensional problem into an NLP. In particular, we chose a *single shooting* approach where we discretised the rope forces along the horizon in N knots equally spaced by $dt = t_f/N$ time intervals and regarded

the states $\mathbf{x}(k) \in [0, N]$ as *dependent* variables, obtaining the following NLP:

$$\min_{\mathbf{U}, \mathbf{f}_{leg}, t_f} \sum_{k=0}^{N-1} \ell(\mathbf{x}_k, \mathbf{u}_k) + \ell_f(\mathbf{x}_N) \quad (27a)$$

$$\text{s.t. } \mathbf{x}_0 = \hat{\mathbf{x}}_0, \quad (27b)$$

$$\mathbf{x}_{k+1} = \mathbf{f}_k(\mathbf{x}_k) + \mathbf{g}_k(\mathbf{x}_k)\mathbf{u}_k, k \in \mathbb{I}_0^{N-1}, \quad (27c)$$

$$\mathbf{h}_k(\mathbf{x}_k, \mathbf{u}_k) \leq 0, \quad k \in \mathbb{I}_0^{N-1}, \quad (27d)$$

We compute the state vector \mathbf{x}_{k+1} from the input \mathbf{u}_k , by integrating the dynamics (27c) via a fourth-order method (i.e. Runge-Kutta 4) starting from the initial state $\mathbf{x}_0 = \hat{\mathbf{x}}_0$. The number of knots N should be roughly adjusted according to an estimate of the jump duration (e.g. by heuristics) in order to reduce the impact of integration errors. Furthermore, to mitigate this issue, we found beneficial to perform integration on a finer grid (cf. paragraph “Integration errors” in Sec. 6.1 for a performance evaluation of different integration schemes). This has the advantage to improve integration accuracy without increasing the problem size.

Boundary Conditions. To start the integration of the dynamics we need to set the initial value for the state:

$$\hat{\mathbf{x}} = [\psi_0 \quad l_{1,0} \quad l_{2,0} \quad \dot{\psi}_0 \quad \dot{l}_{1,0} \quad \dot{l}_{2,0} \quad \mathbf{f}_{leg}]^T. \quad (28)$$

Apart from \mathbf{f}_{leg} that is an optimisation variable that we can arbitrarily set (see the *Initial Guess* paragraph at the end of this section), the other entries can be obtained from the initial robot Cartesian position/velocity.

The inverse kinematics mapping, to convert the robot position \mathbf{p} into \mathbf{q}_r can be obtained with simple geometric analysis:

$$\left\{ \begin{array}{l} \psi = \arctan 2(\mathbf{p}_x, -\mathbf{p}_z), \\ l_1 = \|\mathbf{p} - \mathbf{p}_{a,l}\|, \\ l_2 = \|\mathbf{p} - \mathbf{p}_{a,r}\|, \\ \dot{\phi} = \frac{(\mathbf{n}_\parallel \times \mathbf{n}_\perp)^T \dot{\mathbf{p}}}{(\mathbf{n}_\parallel \times \mathbf{n}_\perp)^T (\mathbf{p}_{a,l} - \mathbf{p}_{a,r})}, \\ \dot{l}_1 = (\mathbf{p} - \mathbf{p}_{a,l})^T \dot{\mathbf{p}}, \\ \dot{l}_2 = (\mathbf{p} - \mathbf{p}_{a,r})^T \dot{\mathbf{p}}, \end{array} \right. \quad (29)$$

where $\mathbf{n}_\parallel = (\mathbf{p}_{a,l} - \mathbf{p}_{a,r}) / \|\mathbf{p}_{a,l} - \mathbf{p}_{a,r}\|$ is the unit vector passing through the anchor points and $\mathbf{n}_\perp = I_{3 \times 3} - \mathbf{n}_\parallel \mathbf{n}_\parallel^T$ perpendicular to the rope plane.

Likewise, for cost and constraint computation, which involve the position/velocity of the robot, these are related to the state variables by means of (4) and its derivative. To avoid overloading the notation, henceforth, we implicitly assume that $\mathbf{p}, \dot{\mathbf{p}}$ are expressed as a function of the state \mathbf{x} . Finally, we wish to enforce that the robot is at the target position \mathbf{p}_{tg} , at the end of the horizon (i.e. end of the jump). The use of hard constraints can prevent convergence when the problem is close to unfeasibility or ill-conditioned. We found it useful to relax the constraint of the terminal state by adding a fixed slack (s):

$$\|\mathbf{p}(t_f) - \mathbf{p}_{tg}\| - s \leq 0. \quad (30)$$

Finally the time t_f is bound to be positive.

State Constraints. State constraints are related to regions of the operation space that are not accessible. A constraint is added to prevent collision with the wall for the whole jump duration

$$\mathbf{n}^T \mathbf{p} \geq \epsilon, \quad (31)$$

where \mathbf{n} is the normal pointing outwards the wall. We set a threshold ϵ to avoid the singular configuration $\mathbf{p}_x = 0$ ($\psi = 0$) for the model (6). To encourage the optimisation to make the robot detach from the wall with a desired clearance $c \in \mathbb{R}$ we force a via point inequality (e.g. at the half of the duration ($t_f/2$) of the trajectory).

$$\mathbf{n}^T \mathbf{p}(t_f/2) \geq c. \quad (32)$$

If the rocky wall has an irregular shape, or there are obstacles that the robot should overcome in order to reach its final destination, the via point constraint should be replaced by one that forces the robot to avoid the obstacle. We can model the inaccessible area as a region whose boundary is a surface. We assume that this surface can be expressed by a smooth 2D manifold expressed by $Q(\mathbf{x}) = 0$. Therefore the admissible region is generally given by $Q(\mathbf{x}) \geq 0$ and could be non-convex.

Actuation Constraints. The rope forces are bounded by the limits of the actuators (e.g. a hoist) and by unilateral constraints:

$$-f_{r,i}^{\max} \leq f_{r,i} \leq 0, \quad i = \{l, r\}. \quad (33)$$

Likewise, the norm of the impulse force \mathbf{f}_{leg} is upper-bounded by the actuation limit:

$$\|\mathbf{f}_{leg}\| \leq f_{leg,\max}, \quad (34)$$

while the unilateral constraint is encoded from its normal component:

$$\mathbf{n}_c^T \mathbf{f}_{leg} \geq 0, \quad (35)$$

where \mathbf{n}_c is the surface normal at the contact location. This can be locally different from the wall inclination \mathbf{n} if there are rock asperities. Additionally, the tangential components of \mathbf{f}_{leg} are constrained by the following second order friction cone:

$$\|\mathbf{t}_x^T \mathbf{f}_{leg} + \mathbf{t}_y^T \mathbf{f}_{leg}\| \leq \mu \mathbf{n}_c^T \mathbf{f}_{leg}. \quad (36)$$

Objective Function. As terminal cost we minimise the final kinetic energy $K(t_f)$ at touch-down. We project the touchdown velocity in the direction normal to the contact location, because it is the one that is getting nullified by the impedance strategy illustrated in Section 5.3. For the running cost we consider 1) a smoothing term for the rope forces, and 2) a second term that penalises the hoist work (i.e. work made to wind/unwind the ropes). Thus, the

cost function is:

$$J = w_s \sum_{k=0}^{N-1} (f_{r,i_k} - f_{r,i_{k-1}})^2 + w_{hw} \sum_{k=0}^{N-1} |f_{r,i} \dot{i}_i| T_s \quad (37)$$

$$+ w_i \underbrace{\frac{1}{2} m \dot{\mathbf{p}}(t_f)^T \mathbf{P} \dot{\mathbf{p}}(t_f)}_{K(t_f)}, \quad i \in \{l, r\}, \quad (38)$$

with w_s , w_{hw} and w_i being the weights associated to the three cost components and $\mathbf{P} = \mathbf{n}_c \mathbf{n}_c^T$ a projection operator to extract the normal component from the velocity $\dot{\mathbf{p}}$.

Initial guess. To speed-up convergence, it is worth to initialise the optimisation with a feasible initial guess. The rope forces are initialised with zeros and the leg impulsive component with $[f_{\text{leg,max}} \ f_{\text{leg,max}} \ f_{\text{leg,max}}]^T$ to easily explore areas away from the singularity. The time t_f is initialised with the time constant for the system linearised around the initial position \mathbf{p}_0 . Note that the linearised system becomes also a reasonable approximation when the jump length is small with respect to the rope elongation.

5. Motion Control

5.1. Flying motion control: Linear position

During the *flight* phase, which starts after the thrusting phase, the leg has no longer influence on the linear motion of the base and the ropes are the only actuators to control the robot's motion. Several factors can make the actual robot position diverge from the planned trajectory (e.g., tracking inaccuracies of the leg impulse, approximations due to the use of the reduced order and environmental disturbances like, for instance, wind). The deviation from the planned trajectory is exacerbated by the presence of strong nonlinearities in the system and can result in unsatisfactory outcomes. For this reason, the presence of a feedback-based motion controller is imperative. The strong changes in the configuration of the system during the flight impede the application of linear strategies around a linearised equilibrium. On the other hand, nonlinear (i.e. Lyapunov-based) approaches are not easy to design in the presence of unilateral constraints (that act as saturation). The presence of saturation constraints also prevents the usage of feedback linearisation approaches. With these considerations in mind, a constrained MPC appeared as the most suitable solution, since it allows to account for several types of constraints. A potential problem with MPC is that, given a nonlinear model, the resulting optimisation problem is non-convex and potentially difficult to solve *online*. Once again, the reduced-order model helps to diminish these problems.

The MPC optimisation problem aims to minimise the tracking error with respect to the optimised reference position \mathbf{p}_{ref} . The decision variables are: 1) the deviations $\Delta \mathbf{F}_{r,l}, \Delta \mathbf{F}_{r,r} \in \mathbb{R}^{2N_{\text{mpc}}}$ of the rope forces with respect to the nominal feed-forward values $\mathbf{F}_{r,l}^*, \mathbf{F}_{r,r}^*$ (the solution of

(27)) and 2) the trajectory of the force $\mathbf{F}_p \in \mathbb{R}^{N_{\text{mpc}}}$ generated by the propeller, where N_{mpc} is the length of the MPC horizon. As for motion planning, the reduced-order dynamics (27c) is integrated to obtain the states (in a single shooting fashion) but this time starting from the *current* state $\hat{\mathbf{x}}$ at sample k . The main differences w.r.t. the offline NLP (27) are that: 1) the MPC is active only during the *flight* phase, hence, the leg impulse is not considered, and 2) we integrate as inputs $\mathbf{F}_{r,i}^* + \Delta \mathbf{F}_{r,i}$ instead of $\mathbf{F}_{r,i}^*$. The resulting optimisation problem is as follows:

$$\begin{aligned} \min_{\Delta \mathbf{F}_{r,\{l,r\}}, \mathbf{F}_p} \quad & w_p \sum_{i=0}^{N_{\text{mpc}}-1} \|\mathbf{p}_{\text{ref}_{k+i}} - \mathbf{p}_i\|^2 + \\ & + w_u \left(\sum_{i=0}^{N_{\text{mpc}}-1} (f_{r,l_i} - f_{r,l_{i-1}})^2 + (f_{r,r_i} - f_{r,r_{i-1}})^2 \right) \\ & + w_{pf} \|\mathbf{p}_{\text{ref}_{k+N_{\text{mpc}}}} - \mathbf{p}_{N_{\text{mpc}}}\|^2, \end{aligned} \quad (39a)$$

s.t.

$$\mathbf{x}_0 = \hat{\mathbf{x}}_k, \quad (39b)$$

$$\mathbf{x}_{i+1} = \mathbf{f} \left(\mathbf{x}_i, \begin{bmatrix} \mathbf{F}_{r,l_{k+i}}^* + \Delta \mathbf{F}_{r,l_i} \\ \mathbf{F}_{r,r_{k+i}}^* + \Delta \mathbf{F}_{r,r_i} \\ \mathbf{F}_p_i \end{bmatrix} \right), \quad i \in \mathbb{I}_0^{N_{\text{mpc}}-1}, \quad (39c)$$

$$-f_{r,\max} \leq \mathbf{F}_{r,l_{k+i}} + \Delta \mathbf{F}_{r,l_i} \leq 0, \quad i \in \mathbb{I}_0^{N_{\text{mpc}}-1}, \quad (39d)$$

$$-f_{r,\max} \leq \mathbf{F}_{r,r_{k+i}} + \Delta \mathbf{F}_{r,r_i} \leq 0, \quad i \in \mathbb{I}_0^{N_{\text{mpc}}-1}, \quad (39e)$$

$$-f_{p,\max} \leq \mathbf{F}_p \leq f_{p,\max} \quad (39f)$$

where k is the index relative to the solution of (27) while i is the index for the MPC trajectory (receding horizon). In the cost function (39b), we included also a regularisation (smoothing term) for $\Delta \mathbf{F}_{r,l}, \Delta \mathbf{F}_{r,r}$. The constraints (39d) and (39e) bound the rope forces, while (39f) bounds the propeller force. Problem (39a) is solved every dt_{mpc} seconds and only the first value is retained from the solution $\Delta \mathbf{F}_{r,l}, \Delta \mathbf{F}_{r,r}$, while the rest is discarded. As common practice, to speed up convergence, we bootstrap each optimisation with the solution of the previous loop. Note that the simulation is running at a much higher rate than the MPC ($dt_{\text{sim}} \ll dt_{\text{mpc}}$) and we apply zero-order hold. When the last sample MPC trajectory matches with the end of the optimal reference trajectory, we start reducing the length of the MPC horizon until the end of the reference trajectory.

5.2. Flying motion control: orientation

In the previous section, we showed how to control the robot Cartesian position during the flight phase, however controlling the orientation is also relevant. To avoid creating undesired moments, the direction of \mathbf{f}_c should point towards the CoM. Tracking errors on \mathbf{f}_c could result in moments that would initiate unwanted pivoting motions. Indeed, this eventually leads to undesirable landing postures (i.e. with landing wheels misaligned with the rock wall), with the risk of tipping over. A solution could be to optimise also for the orientation in (27), but this would

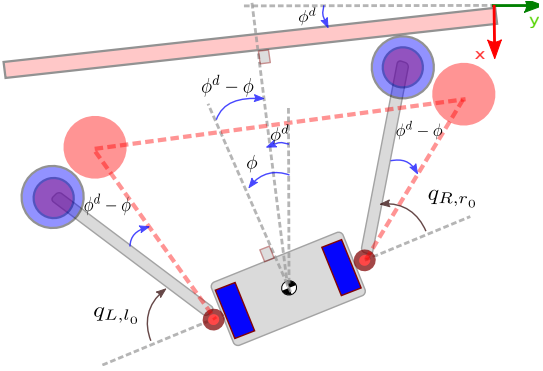


Figure 11: Kinematic strategy for reorientation of the landing system.

require the extension of our simplified model to describe also the angular dynamics.

Leg reorientation. In the case moderate orientation changes are expected, a *kinematic* strategy could be adopted: rather than trying to re-orient the base, we can consider to re-orient both the prismatic leg and the landing mechanism, in order to align them with the wall. Because of the presence of the ropes, most of the times the orientation errors are related to misalignment with the vertical Z axis of the base (see Fig. 4). If we chose a $Z - Y - X$ sequence for the Euler angles to represent orientation, the orientation errors about the Z axis can simply be associated with the tracking error in the yaw direction: $\phi^d - \phi$. To align the prismatic leg and the landing links to the wall, it suffices to continuously adjust their set-points as follows (see Fig. 11):

$$q_{L,i}^d = q_{L,i_0} + (\phi^d - \phi), \quad i \in \{l, r\}, \quad (40)$$

where ϕ is the *actual* value of the yaw angle that can be obtained from the rotation matrix ${}_w\mathbf{R}_b$, which represents the orientation of the base link:

$$\phi = \arctan({}_w\mathbf{R}_{b21}, {}_w\mathbf{R}_{b11}). \quad (41)$$

This approach is meant to have good performance in face of orientation errors up to 0.6 rads. This value is related to the maximum opening of the landing joints, namely, when the landing link is aligned with the base link Y axis.

5.3. Flying motion control: landing

The purpose of the landing mechanism is twofold: 1) to dissipate the excess of kinetic energy at the landing, to avoid bounces and 2) to keep the robot firm on the wall for maintenance operations. During the flight phase, the central *thrusting* leg is retracted and the landing legs are extruded in order to make contact with the wall during the landing phase. At impact, the kinetic energy

$$\tau_{L,i}^d = K_L(q_{L,i}^d - q_{L,i}) - D_L \dot{q}_{L,i}, \quad i \in \{l, r\}, \quad (42)$$

is dissipated through a joint impedance control law implemented for the $q_{L,l}$ and $q_{L,r}$ joints, with stiffness K_L and

damping D_L selected to achieve a critically damped behaviour. The damping value is set considering the reflected inertia of the robot at the joint level. This control strategy avoids the robot bouncing³, thus ensuring a constant contact. For the sake of simplicity, we did not consider the influence of the ropes and gravity force in the impedance law. This is reasonable since, at the impact, the gravity forces and the rope forces are aligned with the landing joint axis; this alleviates their adverse effects on the landing joints (unless the wall is significantly slanted). A more accurate design of a Cartesian impedance controller could be implemented, considering the full (constrained) robot dynamics [42], but this is left for future developments. Notice that, once the joint impedance law takes care of the kinetic energy in the direction perpendicular to the wall, any residual lateral effect can be dissipated with mechanical damping from the landing wheels. When the wall is nearly vertical, the effectiveness of the impedance-based landing strategy diminishes. In such cases, a promising approach could be to activate the propeller to push the robot against the wall, thereby eliminating any potential rebounds.

5.4. Lateral manoeuvring

In situations where the rock wall is free of obstacles (e.g., a clean slab), it is more efficient to navigate the wall locally by actively controlling the motion of the wheels. This approach can also help correct potential landing errors, enabling additional adjustments without requiring further jumps. For the current design, since the wheel is not steerable, only lateral motion is possible. Implementing a wheel-steering mechanism is left for future work. In any case, the motion of the wheels must be coordinated with the motion of the ropes to ensure kinematic consistency. To achieve this, we first compute the mapping (i.e., the Jacobian) between the base link linear $\dot{\mathbf{p}}$ and angular velocity ω_b , and the linear velocities of the landing wheel centres $\mathbf{v}_{l,l}, \mathbf{v}_{l,r} \in \mathbb{R}^3$ ropes $\mathbf{v}_{r,l}, \mathbf{v}_{r,r} \in \mathbb{R}$. Because the wheels $\mathbf{v}_{l,l}, \mathbf{v}_{l,r}$ are constrained to lie along the base axis \mathbf{y}_b , and the ropes velocity vectors lie along the rope axes $\hat{\mathbf{a}}_{r,l}, \hat{\mathbf{a}}_{r,r}$, we can include these constraints in the construction of the Jacobian matrix. Then, referring to the rigid body model and its definitions in Fig. 7, the Jacobian \mathbf{J}_{lm} is a 4×6 and writes:

³A critically damped spring-mass-damper, is a second order system that has no overshoots to a step-response. The impact on the wall can be modelled as a step input to the system and the impedance law act as a virtual spring-mass-damper acting in the direction normal to the wall. Being the contact unilateral to have bounces, it suffices that the velocity of the mass is negative (going out from the wall). The effect of the control law that eliminates overshoots it reflects in the mass velocity being always positive (i.e approaching the wall) eventually becoming zero. This ensure that there is no detachment from the wall (i.e. bounces).

$$\begin{bmatrix} v_{l,l} \\ v_{l,r} \\ v_{r,l} \\ v_{r,r} \end{bmatrix} = \underbrace{\begin{bmatrix} \mathbf{y}_b^T & \mathbf{y}_b^T[-\mathbf{p}_{l,l}] \times \\ \mathbf{y}_b^T & \mathbf{y}_b^T[-\mathbf{p}_{l,r}] \times \\ \mathbf{v}_{r,l}^T & \mathbf{v}_{r,l}^T[-\mathbf{p}_{h,l}] \times \\ \mathbf{v}_{r,r}^T & \mathbf{v}_{r,r}^T[-\mathbf{p}_{h,r}] \times \end{bmatrix}}_{\mathbf{J}_{\text{Im}}} \begin{bmatrix} \dot{\mathbf{p}} \\ \boldsymbol{\omega}_b \end{bmatrix}, \quad (43)$$

where $v_{l,l}, v_{l,r} \in \mathbb{R}$ are scalars representing the velocity of the centre wheels along \mathbf{y}_b axis and the $v_{r,l}, v_{r,r} \in \mathbb{R}$ the rope speed along the rope axes. $[.] \times$ is the skew-symmetric matrix associated to the cross product operator. By setting the desired values $\dot{\mathbf{p}}$ and $\boldsymbol{\omega}_b$ through (43), the set-points $v_{l,l}^d/R_w, v_{l,r}^d/R_w, v_{r,l}^d, v_{r,r}^d$ can be computed. These set-points are then commanded to the PD controllers of the wheel and rope joints, respectively, where R_w is the wheel radius.

6. Simulation Results

This section presents simulation results demonstrating how the proposed solution package enables the robot to navigate along the mountain wall. The goal is to showcase the features outlined in Section 4 and Section 5, which are essential for realizing the use case described in Section 1. Table 1 summarizes the experiments, highlighting the specific features demonstrated in each experiment and indicating which components are active.

6.1. Simulation Setup

We simulate the robot in a Gazebo environment, which computes the full robot (constrained) dynamics using the ODE physic engine [43]. We employ the Unified Robot Description Format (URDF) [44] formalism to describe the robot model and the Pinocchio library [45] to compute the kinematic functions. We always initialise the simulation in a way that the closed loop kinematic constraints are satisfied at the startup (i.e. at a joint configuration \mathbf{q}_{init}).

The optimisation has been implemented in Matlab using the `fmincon` function. To improve performance, we used a C++ implementation of the Optimal Control Problem (OCP) both for motion planning and control, which is freely available⁴.

6.2. Open Loop Model Validation (experiment 1)

As in [23], in a first experiment, we run the optimisation to perform a jump from an initial position $\mathbf{p}_0 = [0.2 \ 2.5 \ -6]^T$ m to a target position $\mathbf{p}_{tg} = [0.2 \ 4 \ -4]^T$ m. We validate the results in open loop for both the reduced model (in a Matlab environment) and the full model (in Gazebo). For the Matlab simulation, we simply integrate (6) with an `ode45` Runge-Kutta variable-step scheme. For the Gazebo simulation, we setup

a state machine that orchestrates the 3 phases of the jump: leg orientation, thrusting and flying. The offline optimisation is run before the leg orientation phase, providing the values of the initial impulse ($\mathbf{f}_{\text{leg}}^*$), the pattern of the rope forces $\mathbf{F}_{r,l}^*, \mathbf{F}_{r,r}^*$ and the jump duration t_f^* . Since the simulation runs at 1 kHz ($dt_{\text{sim}} = 0.001$ s) while the optimised trajectory has a different time discretisation ($d_t = t_f/N$), depending on the jump duration t_f , appropriate interpolations are performed to adapt the rate difference. During the thrusting phase, we generate the pushing impulse \mathbf{f}_{leg} at the CoM by applying a force \mathbf{f}_c at the contact point.

To avoid generating moments at the CoM, we perform a preliminary step (leg orientation phase) to align the prismatic leg to the direction of \mathbf{f}_c . To achieve this, we command the set-points for hip roll and hip pitch joints to be $q_{HR}^d = \text{atan2}(\mathbf{f}_{\text{leg},y}, \mathbf{f}_{\text{leg},x})$ and $q_{HP}^d = -\pi + \text{atan2}(\mathbf{f}_{\text{leg},z}, \mathbf{f}_{\text{leg},x})$. Then, we employ the leg dynamics (last 3 rows of (2)) to map the contact force $\mathbf{f}_c = \mathbf{f}_{\text{leg}}$ into torques $\boldsymbol{\tau}_{\text{leg}}^d$ at the leg joints:

$$\boldsymbol{\tau}_{\text{leg}}^d = \begin{bmatrix} \tau_{HP} \\ \tau_{HR} \\ \tau_K \end{bmatrix} = \mathbf{h}_{\text{leg}}(\mathbf{q}, \dot{\mathbf{q}}) - \mathbf{J}_{c,\text{leg}}^T(\mathbf{q})\mathbf{f}_c, \quad (44)$$

where $\mathbf{J}_{c,\text{leg}} \in \mathbb{R}^{3 \times 3}$ is the sub-matrix of the Jacobian \mathbf{J}_c , whose columns are relative to the leg joints, and $\mathbf{h}_{\text{leg}} \in \mathbb{R}^3$ represents the bias terms (Centrifugal, Coriolis, gravity).

In general, a PD controller is superimposed to the feed-forward torques $\boldsymbol{\tau}_{\text{leg}}^d$ to drive the leg joints q_{HR}, q_{HP}, q_K . However, during the *thrusting* phase, only the feed-forward torques $\boldsymbol{\tau}_{\text{leg}}^d$ are applied, while the PD controller is switched off. Finally, during the *flying* phase, the rope (prismatic) joints are actuated in *force* control mode. The optimised force patterns $\tau_{RP,l}^d = f_{r,l}^*$ and $\tau_{RP,r}^d = f_{r,r}^*$ are set as reference forces for the whole jump duration t_f . During the flight, the landing mechanism and the prismatic leg are continuously reoriented to be always aligned with the wall face, as explained in Section 5.2.

Figure 12 reports the results in *open loop*. Simulating the simplified model, the final error norm is below 0.06 m (due to integration errors), while in the full-model simulation, it is around 0.34 m. These errors are in a range that can be efficiently handled by a controller, as demonstrated in Section 5.1. However, the purpose of this validation is to show that the proposed reduced model is a good approximation of the real system and it is sufficient to generate feasible jumps trajectories that do not involve large orientation changes. Table 2 reports the value of the physical parameters used in the simulation, together with the optimisation settings, that achieve a good compromise between accuracy and convergence rate.

Integration errors. To decrease the computational load of the optimisation process, we can reduce the density of the trajectory's discretisation, which refers to the number of specified points N , also known as knots. This reduction, however, results in integration errors, particularly in single shooting settings. First-order integration methods,

⁴https://github.com/mfocchi/climbing_robots2.git

Table 1: Simulation Experiments

Exp. #	Description	Feature to validate	MPC	Propeller	Land.	Mech.	Fig./Tab.
Exp. 1	Open Loop Model Validation (Sec. 6.2)	Validation of lower dimensional vs. full-detail model					Fig. 12
Exp. 2	Disturbance tests (Sec. 6.3)	Evaluate the capability of the MPC controller to reject disturbances	✓	✓			Fig. 13
Exp. 3	Disturbance tests: Ablation Study (Sec. 6.4)	Evaluate the capability of the MPC controller to reject disturbances without propeller	✓				Fig. 15, 14
Exp. 4	Disturbance tests: Robustness evaluation (Sec. 6.3)	Rejection of random disturbances	✓	✓			Tab. 4, Fig. 16
Exp. 5	Multiple targets (Sec. 6.6)	Test planner capability to do omni-directional jumps	✓	✓			Tab. 5, 6, Fig. 17
Exp. 6	Obstacle avoidance (Sec. 6.7)	Test planner capability to do overcome obstacles of small/medium size	✓	✓			Video only
Exp. 7	Landing test (Sec. 6.8)	Test landing control capability to land without bounces	✓	✓	✓		Fig. 18
Exp. 8	Slanted wall tests (Sec. 6.9)	Test of jump from slanted walls of different inclinations	✓	✓	✓		Only video

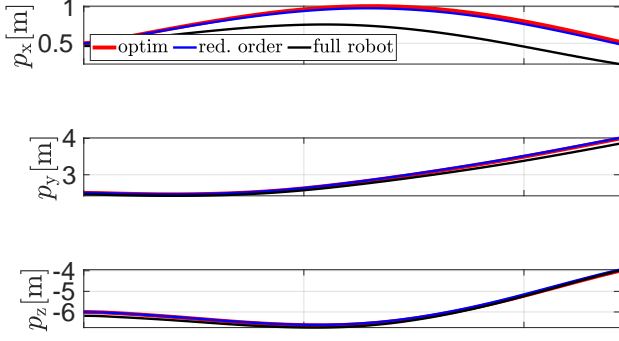


Figure 12: Experiment 1. Open loop validation of the optimisation results. Reference position for the CoM from optimisation (red), simulated trajectory with reduced-order model (blue) and full-robot model (black).

such as Explicit Euler, may not be sufficient to strike a good balance between computational time and accuracy. To improve accuracy, we found beneficial using higher order integration schemes like Explicit Runge-Kutta 4 (RK4) and to perform a number of N_{sub} integration sub-steps of the dynamics within two adjacent knots. We considered that the rope forces remain constant on the time interval dt between two knots.

In Table 3 we evaluate different combinations of: 1) number N of discretisation nodes, 2) number of sub-steps N_{sub} and 3) integration method of different order (Euler or RK4). We benchmark on the same experimental jump employed in validation. We report the number of iterations needed to converge, the solution time, the absolute error at the end of the trajectory with respect to the target $\mathbf{e}_a = \mathbf{p}_{tg} - \mathbf{p}(t_f)$, and the error due to integration $\mathbf{e}_i = \mathbf{p}_{gt} - \mathbf{p}(t_f)$, where \mathbf{p}_{gt} is the final position obtained by integrating with a smaller time step of 0.1 ms. From Table 3 it is evident that both the computation time and the integration error $\|\mathbf{e}_i\|$ are linearly proportional (directly

Table 2: Simulation and optimisation parameters

Name	Symbol	Value
Robot mass [kg]	m	5, 13 (with land. mech)
Anchor distance [m]	d_a	5
Left Anchor position [m]	$\mathbf{p}_{a,l}$	$[0 \ 0 \ 0]$
Right Anchor position [m]	$\mathbf{p}_{a,r}$	$[0 \ b \ 0]$
Friction coeff. []	μ	0.8
Contact normal	\mathbf{n}_c	$[1 \ 0 \ 0]$
Wall normal	\mathbf{n}	$[1 \ 0 \ 0]$
Thrust impulse duration [s]	t_{th}	0.05
Discretisation steps (NLP)	N	30
Simulation time interval [s]	dt_{sim}	0.001
Sub-integration steps	N_{sub}	5
Hoist work weight	w_{hw}	0.1
Smoothing weight	w_s	1
Integration method	-	RK4
Max. (normal) leg force [N]	f_{leg}^{\max}	300, 600 (with land. mech)
Max. rope force [N]	f_r^{\max}	90, 300 (with land. mech)
Jump Clearance [m]	c	1
Slack [m]	s	0.02
Discretisation steps (MPC)	N_{mpc}	50
Tracking term weight (MPC)	$w_{p,\text{mpc}}$	1
Terminal cost weight (MPC)	$w_{pf,\text{mpc}}$	0
Smoothing weight (MPC)	$w_{u,\text{mpc}}$	10^{-5}
Landing wheels radius	R_w	0.075

and inversely) to the number of discretisation points N . Increasing either the number of sub-steps N_{sub} or the order of integration (i.e. using RK4 instead of Euler) makes the single iteration slower but it makes an accuracy improvement; instead, by reducing N , the accuracy decreases. Adding a certain number of integration sub-steps allows to reduce N keeping the accuracy unaltered. Setting N too low the problem can become ill conditioned and convergence might not be achieved. As expected, being RK4 a higher order method, it is superior than Forward Euler in terms of accuracy and requires a lower number of knots N to achieve the same accuracy. As a reasonable trade off, we selected the RK4 with $N = 30$ and $N_{\text{sub}} = 5$ intermediate integration steps.

6.3. Disturbance tests (experiment 2)

To evaluate the effectiveness of the MPC (Section 5.1) in tracking and rejecting disturbances during the flight

Table 3: Performances of different integration schemes

N	Method	N_{sub}	Iters	Comp, Time [s]	$\ \mathbf{e}_i\ $	$\ \mathbf{e}_a\ $
40	RK4	0	44	1.19	0.141	0.148
60	RK4	0	30	1.74	0.045	0.17
40	RK4	5	26	2.1	0.1	0.144
40	EUL	0	28	0.28	0.83	0.85
40	EUL	10	28	1.32	0.05	0.167
30	RK4	5	34	1.71	0.037	0.134

phase, we conducted a test similar to the one of the previous section, but in *closing* the loop with the MPC controller presented in Section 5.1 in presence of disturbances. We set dt_{mpc} equal to the optimal control time step dt and $N_{mpc} = 0.4N$. Since the MPC optimisation takes on average 0.3 s to be computed, to avoid delays in the simulation, we paused the simulation during the optimisation. We postpone to future work a customised C++ implementation more performing than the C++ code generated from Matlab.

Figure 13 presents the tracking plots for the 3 reduced states (ψ, l_1, l_2) when both an impulsive and a constant disturbance are applied to the robot base. The impulsive disturbance is applied after lift-off and persists for 0.2 s, while the constant disturbance is applied during the whole jump. This test has the purpose to emulate the effect of wind⁵. The MPC is able to compensate the impulsive disturbance only after 1.4 s, reaching the target with a cumulative error of 0.072 m. The error during the transient in the impulsive case is related to the presence of the unilateral constraint $(f_{r,i} \leq 0)$, which is hit by the left rope.

Thanks to the predictive capability of MPC, despite the saturation of the control inputs, the tracking error is eventually reduced. Notably, the impulsive disturbance test reveals that the disturbance is more promptly rejected on the ψ variable compared to the other states. This can be attributed to the assumption of having bilateral actuation in the propeller thrust forces (i.e. no unilateral constraint). In the case of constant disturbance, the controller proficiently compensated the disturbance also during the transient, showing a landing error of 0.073 m.

6.4. Disturbance tests: Ablation Study (experiment 3)

In this paragraph, we want to evaluate how performance degrades when the propeller is not present (e.g. a propeller is not installed for cutting costs). We repeated the last tests switching off either the propeller or the whole MPC controller. The results are reported both in Fig. 14 and Fig. 15. The plots reveal that the errors are completely recovered (the MPC controller is still active on the ropes) only on l_1 and l_2 (with a cumulative error of 0.06 m for l_1 and l_2 at landing), while there is a remarkable worsening in the tracking of ψ . This is related to the fact

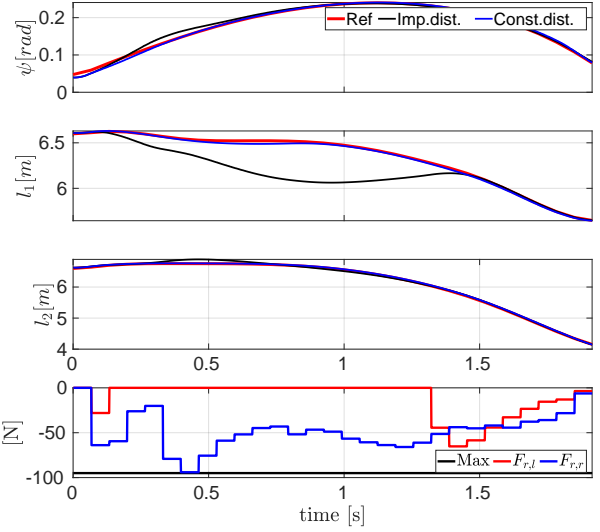


Figure 13: *Experiment 2*. Simulation with MPC. Tracking of the state variables in face of an impulsive $\delta_i = [50, -50, 30]^T$ N (black) and constant disturbance (blue) $\delta_c = [7, -7, 0]^T$ N. The last plot shows the rope forces in the case of the impulsive disturbance.

that the system is under-actuated and the rope forces are constrained on a plane. Therefore, errors on ψ cannot be easily recovered.

6.5. Disturbance tests: Robustness Evaluation (experiment 4)

Impulsive disturbance: In this section, we test the controller under random *impulsive* disturbances applied at different moments of the flight phase. We repeat 100 tests with random disturbances with amplitudes between 25 N and 50 N. We limit the disturbance to a downward hemisphere 1) to avoid unloading the ropes and 2) because it is more representative of a real situation (e.g. rock-falling from above). To quantitatively evaluate the tracking performance during the flight phase, we completely retract the prismatic leg to avoid early or delayed touch-down and let the simulation stop at the end of the horizon ($t = t_f$), where we evaluate the difference between the position of the robot and the desired target. This discrepancy is referred to as the *landing error* \mathbf{e}_a . We discretised the flight phase in 10 intervals of equal duration. For each interval we performed 10 tests applying a randomised disturbance in that interval. In Fig. 16 (left) we report $\|\mathbf{e}_a\|$ as a function of the moment the random disturbance is applied. Since the result can be different for different rope lengths, we tested this for $\mathbf{p}_{tg} = [0.5 \ 4 \ -4]^T$ (short), $\mathbf{p}_{tg} = [0.2 \ 4 \ -9]^T$ (medium) and $\mathbf{p}_{tg} = [0.2 \ 4 \ -12]^T$ (long) jumps, that correspond to rope lengths at the landing of 6, 9 and 12 m, respectively. As expected, the absolute error decreases

⁵Given the form factor of the robot, a 30 km/h wind translates into a 7 N disturbance force.

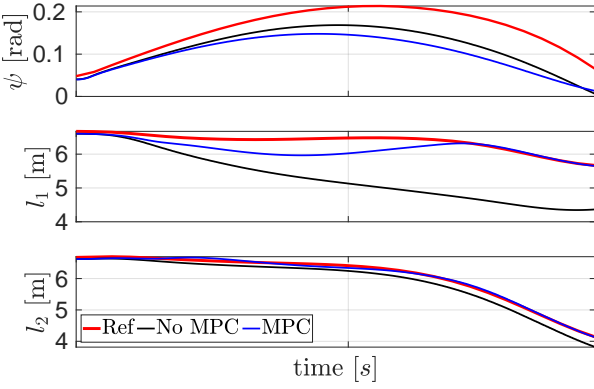


Figure 14: *Experiment 3*. Ablation study. Simulation with **impulsive** disturbance δ_i without propellers.

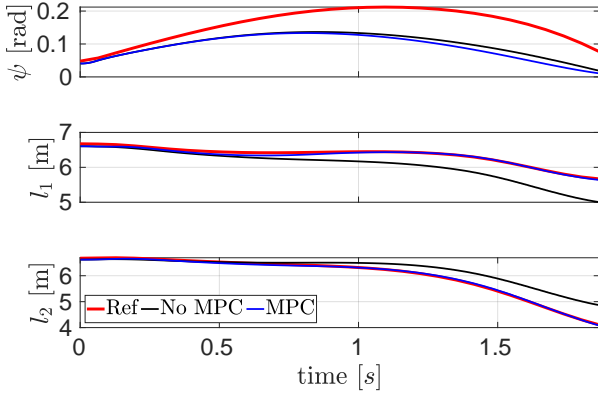


Figure 15: *Experiment 3*. Ablation study. Simulation with **constant** disturbance δ_c without propellers.

with shorter rope lengths but exhibits more erratic behaviour during downward jumps. We hypothesize that this is because the MPC controller has limited room for adjustment when the rope forces approach the upper bound (see the discussion in Section 6.9). Overall, the norm of the absolute error, $\|\mathbf{e}_a\|$, remains constrained within a narrow range, indicating the controller's ability to reject various constant disturbances from different directions.

Constant disturbance: Regarding the constant disturbance, we repeated the experiment for the 6 directions that represent the vertices of a cube, with a constant amplitude of 7 N. The norm of the landing error $\|\mathbf{e}_a\|$ is reported in Table 4. Except for the $[0 \ 1 \ 0]$ direction, they have the same order of magnitude, which is an indicator of the capability of the controller to reject a variety of constant disturbances of different directions. A disturbance in the direction $[0 \ 1 \ 0]$ (Y) is problematic for this specific jump because it would require mainly the action of the left rope to be rejected, which is almost unloaded in the case of the designated landing point \mathbf{p}_{tg} .

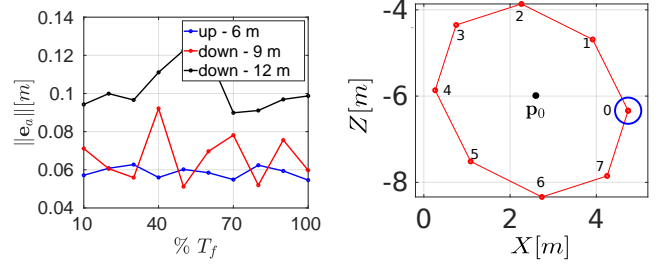


Figure 16: (left) *Experiment 4*. Mean of the norm of the landing error $\|\mathbf{e}_a\|$ for a random impulsive disturbance applied at different moments of the flight phase for jumps involving different rope lengths: short (blue), medium (red) and long (black). The duration of the flight phase is normalised: 0 is lift-off and 100 is touch-down moment. (right) *Experiment 5*. Set of targets to evaluate jumps of variable length and directions. The first target is the rightmost (blue), the others in the list are in CCW order.

Table 4: *Experiment 4*. Tracking errors with constant disturbance

Dist. direction	$\ \mathbf{e}_a\ $ [m]
$[1 \ 0 \ 0]$	0.0512
$[-1 \ 0 \ 0]$	0.0539
$[0 \ 1 \ 0]$	2.4885
$[0 \ -1 \ 0]$	0.2109
$[0 \ 0 \ 1]$	0.0835
$[0 \ 0 \ -1]$	0.1384

6.6. Multiple targets: omni-directional jumps (experiment 5)

We now aim to demonstrate the effectiveness of the control inputs obtained from the *offline* optimisation process presented in Section 4 in manoeuvring the robot to reach various target locations.

It is important to highlight that while we consider the wall to be vertical, a similar approach has also been proven to work for jumps from *non-vertical* (see Section 6.9). To showcase the capabilities of our approach, we have generated a total of 8 target points, evenly distributed on an ellipse around the \mathbf{p}_0 location on the wall. The main axis of the ellipse measures 2.5 m and is inclined at an angle of 45 degrees with respect to the horizontal plane. The minor axis, on the other hand, spans a length of 2 m (refer to Fig. 16(right) for a visual representation). This has the purpose to evaluate how good the optimisation generalises to different jump *lengths* and *directions*. The simulation results are reported in Table 5 and in the accompanying video⁶.

We compute the energy consumption E for each jump, considering the energy consumed in the pushing impulse

⁶Video of experiments available at <https://youtu.be/FqsREaoe-28>

Table 5: *Experiment 5*. Tracking error and energy consumption without hoist work penalisation

Exp.	\mathbf{p}_{tg} [m]	$\ \mathbf{e}_a\ $ [m]	E [J]
0	[0.28 4.73 -6.34]	(0.6) 0.9 ± 0.19	(103) 162 ± 111
1	[0.28 3.91 -4.69]	(0.078) 0.3 ± 0.008	(119) 129 ± 4
2	[0.28 2.26 -3.86]	(0.079) 0.4084 ± 0.16	(200) 147 ± 16
3	[0.28 0.75 -4.35]	(0.081) 1.5 ± 0.95	(287) 607 ± 317
4	[0.28 0.26 -5.86]	(0.066) 0.17 ± 0.007	(228) 199 ± 5
5	[0.28 1.08 -7.51]	(0.067) 0.24 ± 0.06	(261) 214 ± 45
6	[0.28 2.73 -8.34]	(0.08) 0.2653 ± 0.044	(32) 202 ± 71
7	[0.28 4.25 -7.85]	(0.32) 0.62 ± 0.27	(78) 152 ± 108

and in winding/unwinding the ropes:

$$E = \frac{1}{2}m\|\dot{\mathbf{p}}(t_{th})\|^2 + \int_0^{t_f} \left(|f_{r,l}(t)\dot{l}_1| + |f_{r,r}(t)\dot{l}_2| \right) dt, \quad (45)$$

where the former is proportional to the kinetic energy of the robot evaluated at the lift-off ($t = t_{th}$) (assuming the robot starting standstill). The second term is the energy consumed by the hoist motors as the integral of the power along the whole jump duration t_f . The hoist work, in general, dominates. In a first batch of tests we set the weight relative to the hoist work $w_{hw} = 0$ in (38). In another set of experiments we set a non zero weight for the hoist work $w_{hw} = 100$.

To demonstrate the robustness of the approach in a real application where states derivatives are usually obtained by numeric differentiation of encoder readings, we added a zero-mean white Gaussian noise to the state with standard deviation $\sigma = [0.01 \text{ rad/s} \quad 0.2 \text{ m/s} \quad 0.2 \text{ m/s}]$.

Table 5 reports *mean* and *standard deviation* of the norm of the absolute landing error $\mathbf{e}_a = \mathbf{p}_{tg} - \mathbf{p}(t_f)$ and the energy consumption E for each jump. To better appreciate the impact of noise we also report between parenthesis the values without noise. Interestingly, the highest errors are with test 0 and 7, which are the targets that are closer to the vertical of the right anchor (i.e. at $\mathbf{p}_{a,r_y} = 5$ m). This is reasonable because in these tests one of the two ropes is almost unloaded and cannot control properly the error in the Y direction. This suggests that a reduction in performance occurs when one of the ropes is almost unloaded. For the other tests, the error is on average around 0.07 m. The noise results in higher errors with a similar trend, except for test 3, which resulted in a significantly higher average error of 2.22 m. Inspecting the collected data for that target, we noted that the error had an erratic behaviour being very high only in some tests that increase the overall mean, while others are in the same range as 1, 2, 4, 5, 6. We conjecture that this is related to the fact that test 3, being an upward jump, was exceptionally demanding for the left rope that was working at the boundary of its physical actuation limits.

Regarding the consumed energy, this is low for jumps to a lower target (i.e. 6, 7), because the gravity helps and the ropes can be let to passively unwind the ropes to attain the target. However, it was surprisingly high for tests 3, 4, and 5. The reason is that, because there was no penalisation in the cost function, the optimiser found elaborated trajectories to reach the target maximising accuracy disregarding the energy. Therefore, we repeated the previous tests penalising, this time, the hoist work. The results are reported in Table 6.

In this case, the optimiser managed to find solutions that are more energy efficient, with similar accuracy. The trend is

Table 6: *Experiment 5*. Tracking error and energy consumption with hoist work penalisation

Exp.	\mathbf{p}_{tg} [m]	$\ \mathbf{e}_a\ $ [m]	E [J]
0	[0.28 4.73 -6.34]	(0.4) 0.4 ± 0.244	(19.4) 152 ± 125
1	[0.28 3.91 -4.69]	(0.067) 0.068 ± 0.0315	(54) 120 ± 4
2	[0.28 2.26 -3.86]	(0.071) 0.064 ± 0.278	(124) 171 ± 42
3	[0.28 0.75 -4.35]	(0.077) 2.22 ± 1.21	(97) 568 ± 210
4	[0.28 0.26 -5.86]	(0.07) 0.06 ± 0.023	(45) 200 ± 11
5	[0.28 1.08 -7.51]	(0.095) 0.06 ± 0.018	(14) 224 ± 54
6	[0.28 2.73 -8.34]	(0.12) 0.053 ± 0.024	(10) 236 ± 75
7	[0.28 4.25 -7.85]	(0.28) 0.23 ± 0.16	(13) 160 ± 117

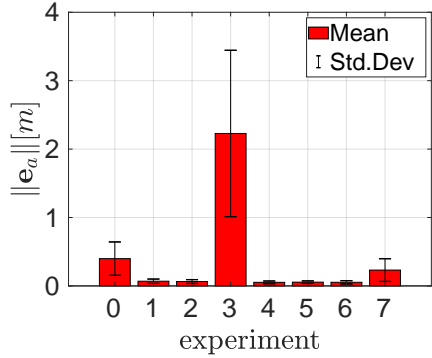


Figure 17: *Experiment 5*. Mean and standard deviation for 50 repetitions of each test in Fig. 16 (with hoist work penalisation) adding white Gaussian Noise to the state derivatives.

now inline with the physical intuition that targets above \mathbf{p}_0 (i.e. 1, 2, 3) are more energy demanding than the ones below (i.e. 5, 6, 7). The impact of noise (c.f. Fig. 17) is similar to the previous case. To highlight the versatility of the approach, in the accompanying video, we conducted additional tests by placing the anchor points at different locations, specifically 5, 7, 9, and 11 meters apart. Despite these varying placements, our optimisation algorithm still successfully produces valid results. We observed that the proposed method yields different solutions for the same target based on the anchor location, yet in all cases a level of landing accuracy comparable with the previous experiments is achieved.

6.7. Obstacle avoidance (experiment 6)

In this section we test capability of the optimal planner to deal with a non-flat wall surface. We model an obstacle as a hemi-ellipsoid whose semi axes are $R_x = 1.5$ m, $R_y = 1.5$ m and $R_z = 0.87$ m, with centre $\mathbf{o} = [-0.5 \quad 2.5 \quad -6]^T$ m⁷. The equation of a generic ellipsoid in standard form writes:

$$\frac{(x - \mathbf{o}_x)^2}{R_x^2} + \frac{(y - \mathbf{o}_y)^2}{R_y^2} + \frac{(z - \mathbf{o}_z)^2}{R_z^2} = 1. \quad (46)$$

To implement obstacle avoidance we set a path constraint $f(\mathbf{x}) > 0$ on the X component of the robot position: $\mathbf{p}_x > \hat{x} + c$. Where c is a clearance margin that should be kept from the

⁷Note, that the obstacle shape is arbitrary. We have already shown in [23] an example with a conic pillar. Any 3D map of the wall face would be suitable given that a convex representation is provided.

obstacle, for safety. $\hat{x} \in \mathbb{R}$ is a function $f(\mathbf{p}_y, \mathbf{p}_z)$ that can be easily obtained from the ellipsoid equation:

$$\begin{aligned}\hat{x} &= \mathbf{o}_x + \sqrt{q}, \\ q &= R_x^2 - \frac{R_x}{R_y}(\mathbf{p}_y - \mathbf{o}_y) - \frac{R_x}{R_z}(\mathbf{p}_z - \mathbf{o}_z)^2.\end{aligned}\quad (47)$$

To ensure that the constraint is enforced only for positions in the convex hull of the ellipsoid (where the square root is defined), we check if the argument q of the square root is positive, otherwise we consider the usual wall constraint (31) where, for vertical wall, $\mathbf{n}^T \mathbf{p} = \mathbf{p}_x$:

$$\begin{cases} \mathbf{p}_x > \hat{x} + c, & q > 0, \\ \mathbf{p}_x > \epsilon, & q < 0. \end{cases}\quad (48)$$

Considering this constraint, and setting a clearance $c = 1$ m, we optimise a jump starting from a point $\mathbf{p}_0 = [0.5 \ 0.5 \ -6]^T$ (to the *left* of the obstacle) to reach a target $\mathbf{p}_{tg} = [0.5 \ 4.5 \ -6]^T$ (to the *right*). The accompanying video shows that the optimisation is able to find a trajectory that allows the robot to successfully overpass the obstacle. We believe the chosen obstacle size is representative of most medium-sized obstacles commonly found in nature and can reasonably be cleared with a single jump. For larger obstacles (e.g., a rock pillar), multiple jumps may be necessary—for example, an initial jump to land on the obstacle, followed by a second jump to surpass it. To explore this scenario, we conducted an additional simulation where the robot jumps onto a taller obstacle (e.g., $R_x = 2.5$ m). One limitation of the actual approach, is that targets that are in the shade cone of the obstacle, could not be reached. This is because the ropes would collide with the obstacle, unless the obstacle is small enough and the ropes come from the sides.

6.8. Landing test and lateral manoeuvring (experiment 7)

Landing: In this section, we conduct a simulation of the robot equipped with the landing mechanism presented in Section 2.1.1 with the aim of assessing the effectiveness of the landing strategy in dissipating any excess kinetic energy during touch-down without causing any rebound. Depending on the accumulated errors during the flight phase, the touch-down could be either early or delayed with respect to the duration of the optimised trajectory. In the case that the touch-down is delayed, we use the feed-forward coming from the optimisation to determine the ropes forces and we apply a gravity compensation action. Due to the additional weight of the lander, in these tests, we increased the mass to 15 kg. This requires that we also ought to adjust the actuation limits: $f_{\text{leg,max}} = 600$ N and $f_{r,\text{max}} = 300$ N. The landing joints $q_{L,f}$ are controlled through the PD strategy (42) with stiffness and damping set to $K_L = 60$ N/m and $D_L = 10$ N/m respectively. Figure 18 reports the tracking of the Cartesian position of the robot for the landing test. It is evident, inspecting the first plot (X variable), that the robot is able to land without re-bounce and that an *early* touch-down occurred.

Lateral Manoeuvring: After the landing, with the purpose to locally explore the area, the controller (43) for lateral manoeuvring is used to drive the robot in a lateral motion, by setting $\dot{\mathbf{p}}^d = [0. \ -0.7 \ 0.]$ m/s $\omega_b^d = [0 \ 0 \ 0]$ rad/s. Additionally, we commanded the propeller to apply 25 N of force to push the robot against the wall, enhancing the grip of the

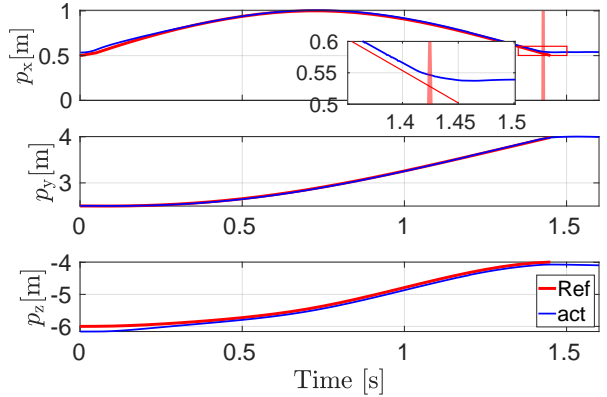


Figure 18: *Experiment 7*. Simulation of the landing test for a wall inclination of 0.1 rad from the vertical. The red and blue plots are the reference and actual position of the robot, respectively. The vertical red shaded line highlights the early touch-down moment.

wheels. The propeller in this case is used solely to enhance contact, as gravity is already counteracted by the ropes, unlike in propeller-wheeled wall-climbing robots, where the propeller must create a bigger normal force such that frictions can overcome gravity [8]. A bottom view of the resulting motion is shown in the accompanying video.

6.9. Jumps on slanted walls (experiment 8)

The presented approach is generic and for any wall inclination within the vertical. Indeed, the wall normal \mathbf{n} is an input for the optimal control planner and can be set according to the value of the inclination of the wall at the lift-off position. In the accompanying video we present results for upward jumps from $\mathbf{p}_0 = [\# \ 2.5 \ -6]^T$ m⁸ to a target position $\mathbf{p}_{tg} = [\# \ 4 \ -4]^T$ m and downward jumps from \mathbf{p}_0 to $\mathbf{p}_{tg} = [\# \ 4 \ -12]^T$ m on slanted walls of different inclinations w.r.t the vertical (0.1, 0.2, 0.3, 0.4 rad). In Table 7 we report the norm of the leg impulse, the energy consumption and the absolute landing error, for the different inclinations of the rock wall for both upwards and downwards jumps.

The output of the optimisation shows that for upward jumps the more slanted is the slope the higher is the impulsive pushing force needed to detach the robot from the rock, because a bigger component of gravity should be overcome. For downward jumps this trend is less evident, on the other hand the energy consumption is significantly lower because the robot mostly exploits gravity to reach the target. In both cases, the tracking error is unaffected by inclination and remains within the same range, whereas it is significantly higher for downward jumps. This occurs because the optimal solution involves rope forces close to the bound $\mathbf{f}_r \leq 0$ N, leaving the MPC with minimal flexibility for corrections. This issue can be mitigated by setting a bound of $\mathbf{f}_r \leq 15$ N. This adjustment provides the MPC with sufficient room to correct model uncertainties,

⁸# indicates that X coordinate is adjusted to be consistent on the wall for the given (Y,Z) pair.

Table 7: Experiment 8. Slanted wall

Jump	Wall incl. [rad]	$\ \mathbf{f}_{\text{leg}}\ [\text{N}]$	$E [\text{J}]$	$\ e_a\ [\text{m}]$
Upward	0.1	98	145	0.074
	0.2	124	166	0.066
	0.3	203	211	0.077
	0.4	230	176	0.067
Downward	0.1	92	30	0.66
	0.2	104	40	0.56
	0.3	90	27	0.67
	0.4	114	33	0.60
Downward	0.1	172	186	0.1
	0.2	285	186	0.072
	0.3	300	178	0.065
$+\mathbf{f}_r \leq 15\text{N}$	0.4	300	189	0.064

reducing the landing errors to values comparable to those observed for upward jumps (see Table 7), at the price of higher leg impulses and energy consumption.

6.10. Energetic comparison with other robotic solutions

In this section we compare ALPINE with existing state of the art solutions in performing maintenance operation. The main requirements for performing maintenance operations are related to power consumption for navigating to a designated destination and remaining stationary on the wall for 30 minutes to carry out the operation (assuming the energy consumed for the operation is the same across all solutions), as well as the travel time needed to reach the target destination. The weight of the operating machine is modelled as a 4 kg payload that the robot must carry in addition to its own weight. The energy consumption will be normalised by the mass of the robot to enable a fair comparison. As a representative navigation we consider again a dislocation from $\mathbf{p}_0 = [0.5 \ 2.5 \ -6]^T$ m to $\mathbf{p}_{tg} = [0.5 \ 4 \ -4]^T$ m. In Table 8, we report the normalised energy consumption for the ALPINE platform, two drones from Nanjing Hongfei Company [46], the lightweight model HZH C680 and the heavy-duty model HZH Y100, the Stickybot III [5], and the ROCR climbing robot [27].

From table 8, an important advantage of roped robots becomes evident, thanks to the brakes that can block the ropes, the energy consumption for standing still on the wall is 0. The consumption of navigation, because gravity is exploited, is very low when descending and higher when ascending. For walking-based climbing robots, energy consumption is also limited, but payload capacity is significantly constrained, and operating speed is relatively slow. A comparison with the two drones demonstrates ALPINE's superior speed, although drones' energy consumption is largely influenced by the hovering time required to remain on-site, which is zero for the climbing robots. Overall, ALPINE combines the best aspects of both types of solutions.

7. Conclusions

This paper presents a robotic platform designed to execute rescue and maintenance operations along mountain slopes. The robot hangs on two ropes that are attached to anchors deployed

on the top of the wall. The motion is guaranteed by two motors that wind and un-wind the ropes, and by a retractable leg that pushes away the robot from the mountain. An auxiliary propeller guarantees the stability of the robot during the flight phases. We have discussed in depth the design of the robot, and shown a simplified dynamic model that captures the dominant components of the system's dynamics, while being mathematically tractable. The model has been used to design motion planning and control strategies based on a suitable MPC formulation. The paper also discusses effective means to compute the locations where the system can be in equilibrium and apply sufficient forces on the wall (e.g., to scale boulders, or perform hammering operations). As an essential part of our work, we also developed a complete and realistic simulation model that we used to collect a large number of simulation results in different application scenarios.

This paper could open the way to a large amount of future work, addressing the problems that this novel platform and its potential applications have unveiled. A non-complete list includes: 1. developing a multi-jump motion planner that considers the hybrid dynamics of the system to plan the system actions across the mode transitions related to the landing-take-off phase; 2. considering a more complete simplified model that accounts for rotational dynamics to improve the control algorithm during the flight phase; 4. investigating the usage of steering wheels for efficient navigation in areas of the wall that are clear of obstacles (e.g., slabs); 3. developing control strategies for specific operations (e.g., drilling scaling) or to deal with harsh and highly uneven terrains; 4. developing learning approaches to enable jumps on crumbly terrain with hardly predictable responses.

References

- [1] A. Nishi, Y. Wakasugi, K. Watanabe, Design of a robot capable of moving on a vertical wall, *Adv. Robot.* 1 (1986) 35–45. doi:10.1163/156855386X00300.
- [2] F. Potenza, C. Rinaldi, E. Ottaviano, V. Gattulli, A robotics and computer-aided procedure for defect evaluation in bridge inspection, *Journal of Civil Structural Health Monitoring* 10 (2020) 471–484.
- [3] J. Seo, L. Duque, J. Wacker, Drone-enabled bridge inspection methodology and application, *Automation in Construction* 94 (2018) 112–126.
- [4] A. Ji, Z. Zhao, P. Manoonpong, W. Wang, G. Chen, Z. Dai, A bio-inspired climbing robot with flexible pads and claws, *Journal of Bionic Engineering* 15 (2018) 368–378.
- [5] E. Hawkes, D. Christensen, M. Cutkosky, Vertical dry adhesive climbing with a 100x bodyweight payload, *Proceedings - IEEE International Conference on Robotics and Automation 2015* (2015) 3762–3769. doi:10.1109/ICRA.2015.7139722.
- [6] M. T. Pope, C. W. Kimes, H. Jiang, E. W. Hawkes, M. A. Estrada, C. F. Kerst, W. R. Roderick, A. K. Han, D. L. Christensen, M. R. Cutkosky, A Multimodal Robot for Perching and Climbing on Vertical Outdoor Surfaces, *IEEE Trans. Robot.* 33 (2017) 38–48. doi:10.1109/TR.2016.2623346.
- [7] W. C. Myeong, K. Y. Jung, S. W. Jung, Y. H. Jung, H. Myung, Drone-type wall-climbing robot platform for structural health monitoring, *Int. Conf. Adv. Exp. Struct. Eng.* 2015-Augus (2015) 1–6.
- [8] K. Sukvichai, P. Maolanon, K. Songkrasin, Design of a double-propellers wall-climbing robot, in: *2017 IEEE International Conference on Robotics and Biomimetics (ROBIO)*, 2017, pp. 239–245. doi:10.1109/ROBIO.2017.8324424.
- [9] M. Alkalla, M. Fanni, A. Mohamed, S. Hashimoto, Teleoperated propeller-type climbing robot for inspection of petro-

Table 8: Normalised energy comparison with state of the art existing solutions

Robot	Weight [kg]	Max Payload Capacity[kg]	Energy navigation[kJ/kg]	Energy stand. still[kJ/kg]	Tot. energy[kJ/kg]	Travel Time[s]
ALPINE	5	$\approx f_r^{\max} / g$	0.03	0	0.03	1.52
Drone - HZH C680 (light-weight) [46]	5	1.5	0.8	83	84	1.5
Drone - HZH Y100 (heavy-duty) [46]	40	100	0.9	75	76	1.5
Stickybot III [24]	1	0.6	0.03	0	0.03	50
ROCR [27]	0.55	0	0.1	0	0.1	17

chemical vessels, *Industrial Robot: An International Journal* 44 (2017) 166–177. doi:10.1108/IR-07-2016-0182.

[10] L. Yang, B. Li, J. Feng, G. Yang, Y. Chang, B. Jiang, J. Xiao, Automated wall-climbing robot for concrete construction inspection, *Journal of Field Robotics* 40 (2023) 110–129. doi:10.1002/rob.22119.

[11] Y. Nishimura, S. Takahashi, H. Mochiyama, T. Yamaguchi, Automated hammering inspection system with multi-copter type mobile robot for concrete structures, *IEEE Robotics and Automation Letters* 7 (2022) 9993–10000. doi:10.1109/LRA.2022.3191246.

[12] S. Qian, B. Zi, W.-W. Shang, Q.-S. Xu, A review on cable-driven parallel robots, *Chinese Journal of Mechanical Engineering* 31 (2018) 1–11.

[13] M. Korayem, H. Tourajizadeh, A. Zehfroosh, A. Korayem, Optimal path planning of a cable-suspended robot with moving boundary using optimal feedback linearization approach, *Nonlinear Dynamics* 78 (2014) 1515–1543.

[14] N. Zhang, W. Shang, S. Cong, Dynamic trajectory planning for a spatial 3-dof cable-suspended parallel robot, *Mechanism and Machine Theory* 122 (2018) 177–196.

[15] S. Newdick, N. Ongole, T. G. Chen, E. Schmerling, M. R. Cutkosky, M. Pavone, Motion planning for a climbing robot with stochastic grasps, in: 2023 IEEE International Conference on Robotics and Automation (ICRA), 2023, pp. 11838–11844. doi:10.1109/ICRA48891.2023.10160218.

[16] S. Lahouar, E. Ottaviano, S. Zeghoul, L. Romdhane, M. Cecarelli, Collision free path-planning for cable-driven parallel robots, *Robotics and Autonomous Systems* 57 (2009) 1083–1093.

[17] M. Polzin, F. Centamori, J. Hughes, Heading for the abyss: Control strategies for exploiting swinging of a descending tethered aerial robot, in: 2023 IEEE International Conference on Robotics and Automation (ICRA), 2023, pp. 5373–5378. doi:10.1109/ICRA48891.2023.10160347.

[18] Webpage, Youbube - Blade BUG: the robot that can repair wind turbines, Accessed on 02/2024. URL: <https://www.youtube.com/watch?v=I3X6Y1F4jAI>.

[19] Webpage, Youbube - Wind Turbine Blade Repairs - Robotics Revolutionizing the Wind Industry, Accessed on 02/2024. URL: <https://www.youtube.com/watch?v=pz9Wn2Kcj4A>.

[20] I. A. Nesnas, J. B. Matthews, P. Abad-Manterola, J. W. Burdick, J. A. Edlund, J. C. Morrison, R. D. Peters, M. M. Tanner, R. N. Miyake, B. S. Solish, R. C. Anderson, Axel and duaxel rovers for the sustainable exploration of extreme terrains, *Journal of Field Robotics* 29 (2012) 663–685. doi:10.1002/rob.21407.

[21] M. Polzin, F. Centamori, J. Hughes, Heading for the abyss: Control strategies for exploiting swinging of a descending tethered aerial robot, in: 2023 IEEE International Conference on Robotics and Automation (ICRA), 2023, pp. 5373–5378. doi:10.1109/ICRA48891.2023.10160347.

[22] L. Wang, U. Culha, F. Iida, A dragline-forming mobile robot inspired by spiders, *Bioinspiration and Biomimetics* 9 (2014). doi:10.1088/1748-3182/9/1/016006.

[23] M. Focchi, M. Bensaadallah, M. Frego, A. Peer, D. Fontanelli, A. Del Prete, L. Palopoli, CLIO: a Novel Robotic Solution for Exploration and Rescue Missions in Hostile Mountain Environments, in: 2023 IEEE International Conference on Robotics and Automation (ICRA), 2023, pp. 7742–7748. doi:10.1109/ICRA48891.2023.10160440.

[24] S. Kim, M. Spenko, S. Trujillo, B. Heyneman, D. Santos, M. R.

Cutkosky, Smooth vertical surface climbing with directional adhesion, *IEEE Transactions on Robotics* 24 (2008) 65–74. doi:10.1109/TRO.2007.909786.

[25] D. K. Riskin, P. A. Racey, How do sucker-footed bats hold on, and why do they roost head-up?, *Biological Journal of the Linnean Society* 99 (2010) 233–240. doi:10.1111/j.1095-8312.2009.01362.x.

[26] A. Parness, N. Abcouwer, C. Fuller, N. Wiltsie, J. Nash, B. Kennedy, Lemur 3: A limbed climbing robot for extreme terrain mobility in space, in: 2017 IEEE International Conference on Robotics and Automation (ICRA), 2017, pp. 5467–5473. doi:10.1109/ICRA.2017.7989643.

[27] S. Jensen-Segal, S. Virost, W. R. Provancher, Rocr: Dynamic vertical wall climbing with a pendular two-link mass-shifting robot, in: 2008 IEEE International Conference on Robotics and Automation, 2008, pp. 3040–3045. doi:10.1109/ROBOT.2008.4543672.

[28] E. M. Hoffman, M. P. Polverini, A. Laurenzi, N. G. Tsagarakis, Modeling and Optimal Control for Rope-Assisted Rappelling Maneuvers, *Proc. - IEEE Int. Conf. Robot. Autom.* 2021-May (2021) 9826–9832. doi:10.1109/ICRA48506.2021.9560802.

[29] A. Coelho, Y. S. Sarkisov, J. Lee, R. Balachandran, A. Franchi, K. Kondak, C. Ott, Hierarchical control of redundant aerial manipulators with enhanced field of view, in: 2021 International Conference on Unmanned Aircraft Systems (ICUAS), 2021, pp. 994–1002. doi:10.1109/ICUAS51884.2021.9476739.

[30] D. W. Haldane, J. K. Yim, R. S. Fearing, Repetitive extreme-acceleration (14-g) spatial jumping with salto-1p, *IEEE International Conference on Intelligent Robots and Systems* 2017-Septe (2017) 3345–3351. doi:10.1109/IROS.2017.8206172.

[31] Q. Nguyen, M. J. Powell, B. Katz, J. D. Carlo, S. Kim, Optimized jumping on the MIT cheetah 3 robot, *Proc. - IEEE Int. Conf. Robot. Autom.* 2019-May (2019) 7448–7454. doi:10.1109/ICRA.2019.8794449.

[32] M. Chignoli, S. Kim, Online trajectory optimization for dynamic aerial motions of a quadruped robot, in: 2021 IEEE International Conference on Robotics and Automation (ICRA), 2021, pp. 7693–7699. doi:10.1109/ICRA48506.2021.9560855.

[33] Y. Ding, M. Zhang, C. Li, H.-W. Park, K. Hauser, Hybrid sampling/optimization-based planning for agile jumping robots on challenging terrains, in: 2021 IEEE International Conference on Robotics and Automation (ICRA), 2021, pp. 2839–2845. doi:10.1109/ICRA48506.2021.9561939.

[34] X. Jiang, W. Chi, Y. Zheng, S. Zhang, Y. Ling, J. Xu, Z. Zhang, Locomotion generation for quadruped robots on challenging terrains via quadratic programming, *Auton. Robots* (2022). doi:10.1007/s10514-022-10068-3.

[35] R. Grandia, F. Jenelten, S. Yang, F. Farshidian, M. Hutter, Perceptual Locomotion through Nonlinear Model Predictive Control, *arXiv* (2022) 1–20. arXiv:2208.08373.

[36] Webpage, Rock schmidt rebound hammer, Accessed on 12/12/2024. URL: <https://www.globalgilson.com/rock-schmidt-hammer-type-n>.

[37] Y. Ding, C. Li, H. W. Park, Kinodynamic motion planning for multi-legged robot jumping via mixed-integer convex program, *IEEE Int. Conf. Intell. Robot. Syst.* (2020) 3998–4005. doi:10.1109/IROS45743.2020.9341572.

[38] R. Orsolino, M. Focchi, C. Mastalli, H. Dai, G. D. Caldwell, C. Semini, Application of wrench based feasibility analysis to the online trajectory optimization of legged robots, *IEEE Robotics and Automation Letters* (2018). doi:10.1109/LRA.2018.2836441.

- [39] V. Delos, D. Teissandier, Minkowski sum of polytopes defined by their vertices, *Journal of Applied Mathematics and Physics* (2015).
- [40] H. Dai, R. Tedrake, Planning robust walking motion on uneven terrain via convex optimization, in: 2016 IEEE-RAS 16th International Conference on Humanoid Robots (Humanoids), 2016, pp. 579–586. doi:10.1109/HUMANOIDS.2016.7803333.
- [41] K. Fukuda, A. Prodon, Double description method revisited, in: M. Deza, R. Euler, I. Manoussakis (Eds.), *Combinatorics and Computer Science*, Springer Berlin Heidelberg, Berlin, Heidelberg, 1996, pp. 91–111.
- [42] E. Mingo, S. Kothakota, A. Moreno, A. Curti, N. Miguel, L. Marchionni, Whole-body kinematics modeling in presence of closed-linkages: application to the kangaroo biped robot, HAL archive, Id: hal-03652472 (2022).
- [43] Russell Smith, Open dynamics engine (ode), <https://www.ode.org/>, 2001. Accessed: 2024-06-17.
- [44] Webpage, URDF Package Summary, Accessed on 02/2024. URL: <http://wiki.ros.org/urdf>.
- [45] J. Carpentier, G. Saurel, G. Buondonno, J. Mirabel, F. Lami-raux, O. Stasse, N. Mansard, The Pinocchio C++ library – A fast and flexible implementation of rigid body dynamics algorithms and their analytical derivatives, in: IEEE International Symposium on System Integrations (SII), 2019.
- [46] Webpage, Nanjing hongfei drones, Accessed on 18/12/2024. URL: <https://nanjinghongfei.en.made-in-china.com>.

8. Appendix*

Definitions of \mathbf{A}_d , \mathbf{b}_d introduced in (6) of the reduced order model.

$$\mathbf{A}_d = \begin{bmatrix} -\mathbf{p}_z & \frac{\mathbf{p}_x}{l_1} - \frac{\sin(\psi)^2 \mathbf{p}_y}{2d_a \mathbf{p}_x l_1} (2l_1^2 - d_a) & \frac{l_2 \mathbf{p}_y \sin(\psi)^2}{d_a \mathbf{p}_x} \\ 0 & \frac{l_1}{d_a} & -\frac{l_2}{d_a} \\ \mathbf{p}_x & \frac{\cos(\psi) \sin(\psi) \mathbf{p}_y}{2\mathbf{p}_x l_1 d_a} (2l_1^2 - d_a) + \frac{\mathbf{p}_z}{l_1} & -\frac{l_2 \mathbf{p}_y \cos(\psi) \sin(\psi)}{d_a \mathbf{p}_x} \end{bmatrix} \quad (49)$$

$$\mathbf{b}_d = \begin{bmatrix} q_1 - \frac{\sin(\psi)^2 q_2}{q_4} - \frac{\mathbf{p}_y 2d_a^2 \sin(\psi) q_1^2}{q_3} + \frac{\dot{\psi} \mathbf{p}_y 2d_a \cos(\psi) q_1}{q_6} + \frac{\dot{l}_1 \mathbf{p}_y 2d_a \sin(\psi) q_1}{q_6 l_1} \\ \frac{-l_2^2 + l_1^2}{d_a} \\ q_7 + \frac{\cos(\psi) q_2}{q_4} + \frac{\mathbf{p}_y 2d_a^2 \cos(\psi) q_1^2}{q_3} - \frac{\dot{l}_1 \mathbf{p}_y 2d_a \cos(\psi) q_1}{q_6 l_1} + \frac{\dot{\psi} \mathbf{p}_y 2d_a \sin(\psi) q_1}{q_6} \end{bmatrix}^T \quad (50)$$

with:

$$\left\{ \begin{array}{l} q_0 = 2\dot{l}_1 \frac{\mathbf{p}_z}{l_1} \dot{\psi} - l_1 \dot{\psi}^2 \frac{\mathbf{p}_x}{l_1} \\ q_1 = -l_2^2 \dot{l}_1 + 2l_1 l_2 \dot{l}_2 - l_1^2 \dot{l}_1 + d_a^2 \dot{l}_1 \\ q_2 = 3\dot{l}_1^2 \mathbf{p}_y 2d_a^2 + 8l_1 l_2 \dot{l}_1 \dot{l}_2 \mathbf{p}_y 2d_a - 2l_1^2 \dot{l}_2^2 \mathbf{p}_y 2d_a + 4l_1^2 l_2^2 \dot{l}_2^2 \\ \quad - 6l_1^2 \dot{l}_1^2 \mathbf{p}_y 2d_a - 8l_1^3 l_2 \dot{l}_1 \dot{l}_2 + 4l_1^4 \dot{l}_1^2 \\ q_3 = \frac{16d_a^4 l_1^2 \mathbf{p}_x^3}{\sin(\psi)^3} \\ q_4 = \frac{4d_a^2 l_1^2 \mathbf{p}_x}{\sin(\psi)} \\ q_6 = \frac{2d_a^2 l_1 \mathbf{p}_x}{\sin(\psi)} \\ q_7 = -\mathbf{p}_z \dot{\psi}^2 + 2\dot{l}_1 \dot{\psi} \frac{\mathbf{p}_x}{l_1} \end{array} \right.$$
